HHS Public Access

Author manuscript

Science. Author manuscript; available in PMC 2016 November 01.

Published in final edited form as:

Science. 2015 April 17; 348(6232): aaa2151. doi:10.1126/science.aaa2151.

Identification and isolation of a dermal lineage with intrinsic fibrogenic potential

Yuval Rinkevich[#1,*], **Graham G. Walmsley**[#1,2], **Michael S. Hu**[#1,2], **Zeshaan N. Maan**[#2], **Aaron M. Newman**[1], **Micha Drukker**[1], **Michael Januszyk**[2], **Geoffrey W. Krampitz**[1], **Geoffrey C. Gurtner**[2], **H. Peter Lorenz**[2], **Irving L. Weissman**[1,3,*], and **Michael T. Longaker**[1,2,*]

[1]Institute for Stem Cell Biology and Regenerative Medicine, Departments of Pathology and Developmental Biology, Stanford University School of Medicine, Stanford, CA 94305, USA.

[2]Hagey Laboratory for Pediatric Regenerative Medicine, Department of Surgery, Plastic and Reconstructive Surgery, Stanford University School of Medicine, Stanford, CA 94305, USA.

[3]Ludwig Center for Cancer Stem Cell Biology and Medicine, Stanford University School of Medicine, Stanford, CA 94305, USA.

[#] These authors contributed equally to this work.

Abstract

Dermal fibroblasts represent a heterogeneous population of cells with diverse features that remain largely undefined. We reveal the presence of at least two fibroblast lineages in murine dorsal skin. Lineage tracing and transplantation assays demonstrate that a single fibroblast lineage is responsible for the bulk of connective tissue deposition during embryonic development, cutaneous wound healing, radiation fibrosis, and cancer stroma formation. Lineage-specific cell ablation leads to diminished connective tissue deposition in wounds and reduces melanoma growth. Using flow cytometry, we identify CD26/DPP4 as a surface marker that allows isolation of this lineage. Small molecule–based inhibition of CD26/DPP4 enzymatic activity during wound healing results in diminished cutaneous scarring. Identification and isolation of these lineages hold promise for translational medicine aimed at in vivo modulation of fibrogenic behavior.

Fibroblasts are the predominant cell type that synthesizes and remodels the extracellular matrix (ECM) in both embryonic and adult organs (1) and are the principal cell type responsible for tissue and organ fibrosis, cutaneous scarring, atherosclerosis, systemic sclerosis, and formation of atheromatous plaques after blood vessel injury (2–5). Numerous

[*]Corresponding author. ryuval@stanford.edu (Y.R.); irv@stanford.edu (I.L.W.); longaker@stanford.edu (M.T.L.).

Author contributions: Y.R. and G.G.W. conceived, designed, and oversaw the experiments, with suggestions from I.L.W. and M.T.L. Y.R., G.G.W., M.S.H., and Z.N.M. performed the experiments and analyzed the data. A.M.N. and M.J. assisted with collection and analysis of data. M.D. assisted with microarray preparations, and A.M.N. analyzed the microarray data. Y.R., G.G.W., M.S.H., and Z.N.M. wrote the manuscript, with helpful suggestions from G.C.G., H.P.L., I.L.W., and M.T.L.

The authors have no competing interests.

SUPPLEMENTARY MATERIALS

www.sciencemag.org/content/348/6232/aaa2151/suppl/DC1

Figs. S1 to S4

Tables S1 and S2

References

studies have investigated the contribution of fibroblasts to the progression of carcinoma (6–9), but, as in the case of wound healing, the identity and embryonic origin of the fibroblasts that contribute to tumor stroma have not been adequately defined. Identifying and prospectively isolating the fibroblast lineage(s) endowed with fibrogenic potential in vivo is an essential step toward effectively manipulating their response to injury across a wide range of acute and chronic disease states.

Here, we identify an embryonic lineage within the dorsal dermis that possesses many of the functional attributes commonly associated with the term “fibroblast.” Despite the presence of other fibroblast lineages in the dorsal dermis, the *Engrailed-1* lineage is the primary contributor to connective tissue secretion and organization during embryonic development, cutaneous wounding, radiation fibrosis, and cancer stroma formation. By identifying and prospectively isolating defined embryonic lineages from skin and oral dermis, we find that fibrogenic properties are cell intrinsic, reflecting inherent functional diversity that exists in cutaneous tissues from different anatomical sites. These findings demonstrate that distinct fibroblast lineages represent unique cell types and take us one step closer to effectively modulating their fibrogenic behavior in vivo.

Results

Multiple lineages of fibroblasts in the dorsal skin

Engrailed-1^{Cre} (*En1*^{Cre}) transgenic mice were crossed with *ROSA26*^{mTmG} (*R26*^{mTmG}) reporter mice (10) to trace the lineage of a population of *En1*-lineage–positive fibroblasts (EPFs), defined in vivo by the expression of green fluorescent protein (GFP), which migrates during embryonic development from the somites into the dorsal trunk dermis (11) (Fig. 1A). To be sure that *Engrailed-1* defines a single embryonic lineage and is not expressed into adulthood, we analyzed its protein and mRNA expression at P1 and P30 in dorsal skin and wounded skin and found absence of expression at these stages (figs. S1, A and B).

Fibroblasts were isolated from the dorsal skin of *En1*^{Cre};*R26*^{mTmG} mice using a fluorescence-activated cell sorting (FACS)–based isolation strategy that allowed for the exclusion of non-mesenchymal lineages (see Materials and Methods) via a lineage negative gate (Lin$^-$). We employed this approach in lieu of a positive selection strategy to be as inclusive as possible and avoid preselection or enrichment of a subpopulation of fibroblasts expressing specific surface markers. This protocol enabled the isolation of uncultured EPFs (defined as GFP$^+$RFP$^-$Lin$^-$) and *En1*-lineage–negative fibroblasts (ENFs) (defined as GFP$^-$RFP$^+$Lin$^-$).

To confirm the validity of our protocol, we performed microfluidic single-cell gene expression analysis of 96 gene targets (table S1) on FACS-isolated EPFs, ENFs, and unfractionated skin cells (as internal controls) from adult (P56) mice. Partitional clustering independently revealed the existence of three transcriptionally distinct cell clusters in dermal tissues, two of which were well represented among labeled cells (termed here as EPFs, ENFs) and one of which was not (Fig. 1B). Compared with the third cluster, the first two were defined by increased expression of “fibroblast” genes such as *Pdgfra*, *Vim*, *P4hb*,

Col1a1, *Col3a1*, and *Fbn1*, as well as decreased expression of *CDH1*, *Epcam*, and *Pecam1* (Fig. 1C). Population-level quantitative real-time polymerase chain reaction (qRT-PCR) analysis of FACS-isolated EPFs, ENFs, and unfractionated skin lysate reinforced these findings, demonstrating that genes associated with nonfibroblast cells (adipocyte, endothelial, neuronal, hematopoietic, muscle, and epidermal) were minimally or not expressed by EPFs and ENFs (Fig. 1D).

Microarray analysis of FACS-isolated uncultured EPFs and ENFs from adult (P56) mice demonstrated that EPFs and ENFs shared a high degree of transcriptome-wide similarity (R^2 = 0.97) (Fig. 2A) and similar expression of fibroblast-related genes—such as vimentin, decorin, and S100A4 (Fig. 2B, left)—and remodeling genes of the ECM (Fig. 2B, right). However, key differences in transcript expression were present, including differential expression of HOXC10, Slit2, Foxp1, leptin receptor (Lepr), myosin light chain kinase (Mylk), and actin alpha 1 (Acta1), among many others (Fig. 2C).

Flow cytometry revealed the existence of two separate population dynamics in vivo. At embryonic day 10.5 (E10.5), EPFs represented less than 1% of total dermal fibroblasts, which at this stage of development were dominated by ENFs (95.5% of dermal fibroblasts). With time, EPFs increased from 22.2% of total dermal fibroblasts at E16.5, to 42.9% at P1, and to 75.3% of total dermal fibroblasts at P30 (Fig. 2D), with similar percentages of EPFs/ENFs at subsequent post-natal stages (P56).

EPFs and ENFs, sorted from embryonic (E16.5) and adult (P30) mice, and cultured in vitro, displayed similar spindle-shaped morphology characteristic of fibroblasts (Fig. 2E). The cells were highly motile, stained positive for markers classically associated with fibroblasts, such as fibroblast-specific protein 1 (FSP-1) and vimentin, as well as expressing components of the ECM, including type I collagen and fibronectin (Fig. 2F), and were negative for epithelial (keratin 5/14), neural (neurofilament NF-H), adipocytic (adiponectin), endothelial (CD31), and hematopoietic (CD45) markers (fig. S1C).

Fibrogenic potential of dermal fibroblasts is lineage-restricted

Next, we performed lineage-tracing analysis using $En1^{Cr};R26^{mTmG}$ mice. Upon histologic analysis of dorsal skin from $En1^{Cr};R26^{mTmG}$ mice, we observed labeling of dermal ECM with the fluorescent protein expressed on the surface of the cell responsible for depositing those ECM components (Fig. 3, A to C). At E10.5, ENFs comprised the entirety of the developing dermis, and RFP signal labeled all cells and dermal ECM (Fig. 3B, top panel). At E12.5, EPFs were observed localizing to the papillary dermis only (Fig. 3B, second panel). Subsequently, at E16.5, EPFs appeared to migrate to the lower reticular dermis (Fig. 3B, third panel), complete their migration at P1, and maintain a presence there throughout postnatal stages of development (Fig. 3B, bottom panel, and Fig. 3C). Consequently, the majority of the deposited connective tissue within the underlying dermis, the stroma associated with dermal pegs, the stroma surrounding hair follicles, and dermal papillae (Fig. 3, B and C) was GFP-positive and hence EPF-derived.

To confirm that the observed ECM fluorescence correlated with the deposition of ECM components, dorsal dermis from adult (P30) $En1^{Cr};R26^{mTmG}$ mice was stained for the

predominant collagens (types I and III) in cutaneous dermis (12), which displayed an overlapping pattern with GFP fluorescence (Fig. 3D, top and middle panel). In contrast, keratin 14, a marker for basal keratinocytes and hair follicle epithelium, displayed a nonoverlapping pattern with GFP fluorescence (Fig. 3D, bottom panel). These results indicate that, while at least two separate embryonic lineages of fibroblasts exist within the dorsal dermis, only EPFs function in vivo as effectors of connective tissue secretion and formation.

Analysis of wounded and unwounded dorsal dermis in uncrossed $R26^{mTmG}$ mice demonstrated the presence of RFP in all connective tissue fibers within the dermis (fig. S1D) in a pattern identical to that of GFP in the dorsal dermis of $En1^{Cre};R26^{mTmG}$ mice (Fig. 3, C and E), ensuring that our findings were not a result of difference in emission intensities between membrane-bound GFP and RFP in connective tissue stroma. As expected, dorsal cutaneous wounds in $Tie2^{Cre};R26^{mTmG}$ (endothelial and hematopoietic lineages) and $K14^{Cre};R26^{mTmG}$ (epithelial lineage) mice were completely negative for GFP-labeled connective tissue (fig. S1E, top two panels). These results demonstrate that ECM deposition in the dorsal skin is a property unique to EPFs, with absence of any contributions from hematopoietic, endothelial, or epithelial cell lineages.

We analyzed the dermis of *FVB-Tg(CAG-luc,-GFP)L2G85Chco/J(L2G)* mice, which express cytoplasmic enhanced GFP (eGFP) constitutively in all cells (13) and found that in marked contrast to the $R26^{mTmG}$ system, GFP fluorescence within the dorsal dermis of adult *L2G* mice was localized to dermal cells, epidermis, and hair follicle epithelium (fig. S1E, third panel), but did not label the dermal ECM to the degree seen in $En1^{Cre};R26^{mTmG}$ mice (Fig. 3C). Furthermore, GFP fluorescence highlighted individual stromal and vascular cells within scar tissue from 6-mm excisional wounds induced on the dorsal backs of adult *L2G* mice at 12 to 14 days after wounding but did not label deposited connective tissue and ECM components (fig. S1E, bottom panel).

Given the important role of EPFs in connective tissue secretion during embryonic and postnatal development, we next assessed the relative contributions of EPFs and ENFs to scar formation after cutaneous wounding in the dorsal skin of adult (P30) $En1^{Cre};R26^{mTmG}$. The majority of the deposited scar tissue was GFP-positive and hence EPF-derived (Fig. 3E). Moreover, collagen type I protein expression within the scar site displayed an overlapping pattern with GFP fluorescence, implicating EPFs as the primary secretors of collagen in the healing wound (fig. S1F). We repeated this analysis using a humanized model of wound healing, which proceeds through granulation tissue formation and re-epithelialization, with minimal contraction. Tissues harvested at 14 days after wounding showed abundant EPF-derived collagen filaments and connective tissue (fig. S1G), indicating that regardless of the primary mechanisms underlying wound closure, and despite the presence of ENFs in the healed dermis (Fig. 3F), EPFs are responsible for the bulk of ECM deposition after injury of the dorsal skin in adult mice.

To assess the possibility of a migratory cell lineage contributing to ECM deposition, including the migratory capacity of EPFs, we performed parabiosis between $En1^{Cre};R26^{mTmG}$ and background strain (*B6*) mice. After 2 months, excisional skin wounds

were induced on the dorsum of the *B6* strain mice. After 14 days, wounds were harvested and analyzed for GFP/RFP fluorescence. We found only scattered donor-derived RFP^+ cells in the wound site, with a complete absence of both RFP^+ ECM and GFP^+ cells (fig. S1H). The absence of GFP^+ cells and RFP signal from wound connective tissue/ECM indicates that EPFs are not capable of migrating through the circulation to wound sites and that migratory RFP^+ cells were not directly contributing to scar formation/connective tissue deposition. To further rule out a connection between the EPF lineage and a migratory/circulatory hematopoietic niche, we harvested bone marrow from adult $En1^{Cre};R26^{mTmG}$ mice and found a complete absence of GFP signal within the marrow (fig. S1I).

Fibrosis can also occur in a slowly developing reactive process, such as the stromal response to radiation (14) or carcinoma, particularly malignant melanoma (15). B16 mouse melanoma cells were transplanted to the dorsum of $En1^{Cre};R26^{mTmG}$ mice, and after 30 days, tumors were harvested for histology. Consistent with previous reports (16, 17), we found multiple host-derived cells within the melanoma tumor, including various hematopoietic cell types, blood vessels, and fibroblasts surrounded by connective tissue stroma. The stroma of the melanoma was predominantly EPF-derived (GFP^+) (Fig. 3G). To be sure that Engrailed-1 was not expressed in response to tumor cells, we stained tumor stroma sections for *Cre* and found no expression (fig. S1J). As a positive control, *Cre* was expressed in E11.5 $En1^{Cre};R26^{mTmG}$ dorsal skin sections, as expected (fig. S1J).

We next explored the contribution of EPFs versus ENFs to connective tissue deposition during radiation-induced fibrosis of the skin. Irradiated skin was harvested on day 14 and showed gross signs of radiation-induced fibrosis, including erythema and leathery skin. Histologic analysis revealed a significant fibrotic response with primarily EPF-derived ECM and an absence of ENF-derived ECM (fig. S1K). All blood vessels and hematopoietic infiltrates within the fibrotic tissue were RFP-positive, as expected. These data further demarcate EPFs as the primary lineage contributing to connective tissue deposition during embryonic development, postnatal wound healing, cancer stroma formation, and radiation fibrosis of the skin.

Fibrogenic potential of dermal fibroblasts is cell-intrinsic

To investigate whether differences in wound repair between oral and cutaneous dermis (18) are a consequence of cell-intrinsic versus environmental properties, we analyzed the contribution of the embryonic neural crest to the cranial and oral dermis, using the $Wnt1^{Cre}$ transgenic mouse, which permanently labels early migratory neural crest populations at all axial levels (19–21). The oral dermis from $Wnt1^{Cre};R26^{mTmG}$ was harvested, and *Wnt1* lineage–positive fibroblasts (WPFs), defined in vivo by their GFP positivity (and $GFP^+RFP^-Lin^-$ by flow cytometry), were present within oral dermis and exhibited a significant contribution to connective tissue secretion and organization, as seen by GFP signal that labeled the dermal ECM (Fig. 4A).

However, a population of *Wnt1* lineage–negative fibroblasts (WNFs, defined as $GFP^-RFP^+Lin^-$ by flow cytometry) was also present within the oral dermis, as seen by histology and FACS analyses (Fig. 4, A and B). FACS-isolated WPFs and WNFs both exhibited spindle-shaped morphologies and were highly motile (Fig. 4C). These results

indicate that, similarly to cutaneous sites, at least two separate lineages of fibroblasts coexist within the oral dermis (WPFs defined as $GFP^{+}RFP^{-}Lin^{-}$ and WNFs defined as $GFP^{-}RFP^{+}Lin^{-}$), out of which only WPFs are the primary contributing lineage to ECM deposition in vivo.

Given the role of WPFs in connective tissue secretion and organization of the oral dermis during postnatal development (Fig. 4A), we hypothesized that WPFs contribute significantly to connective tissue deposition within the oral cavity after wounding. Full thickness wounds in the buccal mucosa of adult (P30) $Wnt1^{Cre};R26^{mTmG}$ mice displayed a beehive pattern of collagen deposition within the dermis and a characteristic epidermal hyperproliferation of keratinocytes (Fig. 4D). The majority of the deposited scar tissue was GFP-positive and hence WPF-derived (Fig. 4D). The architecture of these oral scars differed significantly from the dense plugs of connective tissue seen in cutaneous dorsal scars (Fig. 3E). Consistent with this difference in scar architecture, collagen content was significantly diminished within oral wounds in comparison with dorsal skin wounds (Fig. 4E), as seen by decreased blue (collagen) staining with Maisson's trichrome.

To begin investigating the intrasite and intersite diversity in fibroblast heterogeneity, we compared the transcriptional programs of EPFs isolated from dorsal and ventral dermal sites of adult (P30) mice to those of WPFs from cranial and oral dermal sites of adult (P30) mice, using gene expression microarray analysis. Unsupervised clustering using AutoSOME (22) revealed groups of coordinately expressed genes underlying similarities and differences among the fibroblast populations (Fig. 4F), with the most notable differences identified between EPFs and WPFs (fig. S2A). Indeed, although each of the four populations (dorsal, ventral, cranial, and oral cavity) is readily distinguishable by transcriptome-wide expression analysis ($P < 0.05$; AutoSOME clustering), EPFs and WPFs exhibit the highest degree of difference in global expression signatures (Fig. 4G), consistent with their separate somitic and neural crest origins.

To directly assess whether site-specific differences in dermal architecture reflect cell-intrinsic properties of distinct fibroblast lineages (*Wnt1* neural crest derived versus *Engrailed-1* somitic derived) or are an outcome of distinct anatomic microenvironments, we initiated reciprocal transplantation experiments. Ten days after transplantation, both sites (oral cavity and dorsal back) revealed ectopic deposition of connective tissue that was donor-cell derived (GFP^{+}). However, the EPF-derived scar tissue deposited within the oral cavity was significantly different from host-derived ECM, with dense and elongated collagen fibrils, minimal infiltrate of vasculature or hematopoietic cells, and exhibited classic dorsal scar phenotypes (Fig. 4H). Although similar cell numbers were transplanted in both experiments (1×10^5), WPFs transplanted into the dorsal back exhibited considerably reduced scarring in comparison with EPFs transplanted into the oral cavity, as seen by GFP fluorescence and collagen type I staining (Fig. 4H, bottom panels). Instead of forming a dense plug of scar tissue, as seen by EPFs transplanted into the oral cavity, WPFs were dispersed around hair follicles, where they secreted a beehive pattern of collagen deposition (Fig. 4H, bottom panels), mimicking a minimal oral cavity scar (Fig. 4, D and E). We found no significant difference at 10 days after transplantation, in either cell proliferation or cell survival parameters between EPFs transplanted into the oral cavity and WPFs transplanted

into the dorsal dermis ($n = 5$) (fig. S2, B and C). These data indicate that WPFs and EPFs are functionally distinct populations in terms of their migratory and secretory programs.

Cycles of growth and rest phase of hair follicles within the dorsal skin cause cyclic change in dermal thickness (23). To investigate whether these changes may affect the ECM deposition of implanted cells, we transplanted WPFs (1×10^5) to the dorsal back skin of mice at 4 and 7 weeks of age, representing anagen and telogen phases of the hair follicle cycle, respectively. We found no difference in collagen distribution pattern in relation to hair follicle cycle ($n = 5$) (fig. S2D). These data indicate that site-specific differences in dermal architecture between oral and cutaneous dermis are predominantly outcomes of lineage-intrinsic properties that are unaffected by new host tissue, regardless of anatomic location, dermal age, or hair follicle cycle.

DTR-based ablation of EPFs reduces cutaneous scarring during wound healing

Given the role of EPFs as the primary lineage responsible for cutaneous scar deposition, we next investigated whether ablation of the lineage could lead to a reduction in scarring.

We crossed $R26^{tm1(HBEGF)Awai}$ mice, which express simian diphtheria toxin receptor (DTR) in a Cre-dependent manner, with $En1^{Cre};R26^{mTmG}$ mice. The resulting triple-positive offspring ($En1^{Cre};R26^{mTmG};R26^{tm1(HBEGF)Awai}$), expressing both GFP and DTR in EPFs only, were dorsally wounded and were treated with either 200-ng diphtheria toxin (DT) in phosphate-buffered saline (PBS) or PBS alone (control).

Wound size in DT-treated mice increased from day 0 to day 3 of wounding (Fig. 5A), implicating EPFs as the predominant lineage from which contractile, scar-forming myofibroblasts are derived. Complete healing of DT-treated wounds required 20 days, an additional 6 days over that of control wounds (14 days) and reported splinted excisional wound healing rates (24) in mice (Fig. 5B). Endpoint analyses were therefore conducted on fully healed DT-treated and control wounds harvested at 21 days and 15 days after wounding, respectively.

Scar size, measured as a percentage of initial wound size, was not significantly different in DT-treated as compared with control wounds ($P = 0.3192$) (Fig. 5C). However, histologic analysis revealed greatly reduced GFP-labeled connective tissue deposition in DT-treated as compared with PBS-treated controls (Fig. 5D). Moreover, the overall pattern and density of collagen deposition differed markedly between DT-treated and control wounds. Maisson's trichrome staining revealed greater cellularity and reduced collagen density, evidenced by a higher ratio of red to blue staining, in treated as compared with control wounds (Fig. 5E). The change in collagen deposition did not influence the tensile strength of the healed wounds (Fig. 5F) or result in regeneration of adipocytes or hair follicles in the healed dermis (Fig. 5, G and H). Taken together, these data confirm an important functional role for EPFs both in terms of wound closure and connective tissue deposition during wound healing.

DTR-based ablation of EPFs reduces melanoma growth

Given our finding that EPFs are the primary fibroblast lineage responsible for dermal fibrosis seen in cutaneous melanoma, we next assessed the effects of ablating EPFs before

melanoma growth. Tumors were allowed to grow in DT-treated ($n = 10$) and control ($n = 10$) mice until euthanasia was dictated by protocol parameters for a single mouse, at which point all mice were killed for endpoint analyses. Tumor burden (as measured by total tumor weight at day 22) was significantly higher ($P = 0.0166$) in control melanomas than in DT-treated melanomas (Fig. 5I). Histologic analysis of GFP/RFP fluorescence revealed reduced deposition of EPF-derived (GFP^+) connective tissue in DT-treated as compared with control melanomas (Fig. 5J). As expected, deposition patterns in the control-treated melanomas of $En1^{Cre};R26^{mTmG};R26^{tm1(HBEGF)Awai}$ mice (Fig. 5J) closely resembled those seen in $En1^{Cre};R26^{mTmG}$ mice transplanted with melanoma (Fig. 3G).

Surface profiling and prospective isolation of EPFs

Having identified EPFs as a fibrogenic lineage in the dorsal dermis and established their functional importance through DTR-based ablation, we endeavored to prospectively isolate EPFs from the dermis of wild-type mice using flow cytometry methods. As before, a FACS-based fibroblast purification strategy using a lineage-negative gate (Lin^-) was employed to isolate EPF and ENF populations for all experiments discussed here. Adult mice aged 8 weeks were used.

Both surface markers currently proposed for fibroblast isolations—including CD44, CD90 (Thy1), biglycan, CD73 (fig. S2E)—and 35 additional surface molecules that were identified based on a whole-transcriptome microarray data of uncultured EPFs and ENFs (fig. S3) were expressed on both EPFs and ENFs, precluding them as discriminatory surface molecules. We employed a cell surface marker screen composed of 176 monoclonal antibodies to assess the presence and relative abundance of each surface molecule on EPFs and ENFs. FACS analysis revealed that most of the 176 surface molecules in the screen were either marginally expressed on both populations or were present on both populations to similar degrees (table S2). For example, CD13 was expressed on both EPFs (35.2%) and ENFs (28.7%). CD34, a transmembrane glycoprotein thought to be involved in the modulation of signal transduction and cell adhesion (25), was broadly expressed on EPFs (75.6%) and ENFs (50.5%). CD47, a surface molecule known to interact with macrophages and inhibit apoptosis (26), was expressed on a greater percentage of EPFs (65.5%) than ENFs (24.1%). Thus, although these molecules cannot be used to uniquely identify or substantially enrich for EPFs over ENFs, their presence on large fractions of EPFs indicates that they may hold functional importance. The commonly cited fibroblast marker Thy1 (CD90) was expressed broadly within both EPF and ENF populations and therefore was ineffective as a discriminatory lineage marker, consistent with our whole-genome and flow cytometry analysis (table S2).

From the list of 176 surface molecules, we identified several markers that were highly expressed on EPFs and marginally on ENFs (CD26, LY-51, CD54, and CD61) (table S2). FACS analysis of primary noncultured EPFs and ENFs isolated from $En1^{Cre};R26^{mTmG}$ mice identified CD26 as the surface marker offering the highest-fold enrichment of EPFs over ENFs (nearly 15-fold) (fig. S4A) and labeled a large percentage of EPFs (94%) (Fig. 6A). The fold enrichment and purity of EPFs achieved with CD26 significantly surpassed those of the classic fibroblast markers previously described, such as CD73, CD90, and biglycan,

which either did not enrich for EPFs (CD90 and biglycan) or were limited to a maximum enrichment of 3.5-fold (CD73) (fig. S2E). WPFs were found to express CD26 at levels similar to EPFs (fig. S4B).

To further confirm the presence and specificity of these markers on EPFs in situ, we performed immunohistochemical analyses on dorsal dermis from P30 $En1^{Cre};R26^{mTmG}$ mice. Consistent with FACS analyses, high CD26 immunopositivity was observed in regions of upper dermis between hair follicles, but not on the follicles themselves, and displayed an overlapping pattern with GFP but not RFP fluorescence (Fig. 6B). Furthermore, although CD26 has been reported to be a specific marker for upper dermis during fetal development (27), it appears that CD26 is also expressed in the lower reticular dermis during adult stages (Fig. 6B).

To functionally corroborate that possibility, $CD26^{+}Lin^{-}$ and $CD26^{-}Lin^{-}$ fibroblast populations from uncrossed $R26^{mTmG}$ transgenic mice, representing EPFs and ENFs, respectively, were FACS-sorted and transplanted via intradermal injection into the dorsal backs of immunodeficient $RAG\text{-}2^{-/-}$ double-knockout mice. Intradermal injection induces an initial inflammatory response followed by fibrosis (scarring) and was therefore chosen as an in vivo assay for ECM deposition.

Histologic analysis of grafted cells at 10 days after transplant revealed a dermal architecture with abundant deposition of RFP-labeled ECM in the CD26-positive grafts that was nearly absent in the CD26-negative grafts (Fig. 6C). Despite approximately equal numbers of total RFP^{+} cells, the increased and more diffuse pattern of RFP-labeled ECM is evident in skin transplanted with CD26-positive as compared with CD26-negative fibroblasts (Fig. 6C). RFP signal was found to be significantly higher in CD26-positive as compared with CD26-negative grafts (Fig. 6C). qRT-PCR analysis of RFP-positive cells FACS-sorted 10 days after transplant from $CD26^{+}Lin^{-}$ and $CD26^{-}Lin^{-}$ grafts revealed 5.32-fold greater expression of collagen type I (collagen type in cutaneous scars) and 7.11-fold greater expression of alpha-smooth-muscle actin (a marker of fibroblast activation) in CD26-positive grafts than in CD26-negative grafts (Fig. 6D, left). At baseline, this difference is markedly reduced, suggesting that, although $CD26^{+}$ EPFs and $CD26^{-}$ ENFs have similar expression of ECM genes, their ability to respond to stimuli and up-regulate the expressions of ECM and contractile genes is one major molecular difference between these populations (Fig. 6D, right). Together, these findings functionally corroborate CD26 as a marker for a distinct fibrogenic lineage in the dorsum of mice.

Given the fibrogenic contributions of EPFs to melanoma progression in the dorsal backs of $En1^{Cre};R26^{mTmG}$ mice (Fig. 3G), we investigated the contribution of the $CD26^{+}Lin^{-}$ versus $CD26^{-}Lin^{-}$ fibroblasts to the stromal compartment of melanomas. Primary fibroblasts were sorted from the dorsal dermis of uncrossed $R26^{mTmG}$ reporter mice based on their membrane expression of CD26 and cotransplanted with B16 F10 mouse melanoma cells by intradermal injection into the dorsal skin of $RAG\text{-}2^{-/-}$ double-knockout mice. After 30 days, histologic analysis of the transplanted tumors revealed a dermal fibrotic phenotype with increased deposition of RFP-labeled ECM in melanomas cotransplanted with $CD26^{+}Lin^{-}$ fibroblasts in comparison with melanomas cotransplanted with $CD26^{-}Lin^{-}$ fibroblasts (Fig.

6E). These data functionally corroborate CD26 as a surface marker for a fibroblast lineage responsible for ECM deposition after cutaneous injury and melanoma stroma formation.

Inhibition of CD26 reduces cutaneous scarring during wound healing

CD26, also known as dipeptidyl peptidase-4 (DPP4), is a cell-surface serine exopeptidase that cleaves X-proline dipeptides from the N terminus of polypeptides (28). Given the selective expression of CD26 on the surface of scar-forming EPFs, we next assessed the effects of inhibiting CD26 on scar formation during wound healing using a small molecule (diprotin A), which acts as a selective allosteric inhibitor of CD26 peptidase activity through its function as a slowly hydrolyzed substrate for CD26 (29).

The rates of healing between treated and control wounds during the initial days of wound healing remained approximately equal. However, a significant difference in wound size of ~30% developed by day 9 after wounding, with larger and less healed wounds in CD26-inhibitor–treated cohorts in comparison with controls (Fig. 6F). This difference persisted through the remaining days of wound healing. Ultimately, complete healing of CD26-inhibitor–treated wounds took 5 days longer ($P < 0.01$) than control wounds (Fig. 6F). Most important, although the rate of healing was decreased in inhibitor-treated versus control wounds, treated wounds showed significantly reduced final scar size ($P < 0.001$) after wound healing had reached completion as a percentage of the original wound size in comparison with control wounds (Fig. 6, G and H).

Discussion

Fibroblast functional properties: Intrinsic or extrinsic?

A critical question concerning fibroblast biology is whether their specific functional properties are cell-intrinsic or cell-extrinsic. Our reciprocal transplantation experiments showed that differences in dermal architecture and wound healing outcomes between oral versus dorsal dermis are independent of the local microenvironment and can be mimicked by transplantations of distinct fibroblast lineages, indicating that cell-intrinsic properties rather than environmental differences are the primary effecting mechanisms underlying intersite diversity.

A recent study also lends support to this notion. Driskell *et al.* identified a distinct lineage of fibroblasts involved in forming the embryonic dermal architecture (27). Our data, along with that of Driskell *et al.*, begin to define fibroblast lineages that have different roles in skin development, homeostasis, and response to acute or chronic injury. The analysis of the Driskell *et al.* report and our data implies that embryonic lineages of fibroblasts represent de facto operational hierarchies that underlie the diversities of regenerative programs and outcomes between anatomic sites.

Our data describing the fibroblast lineages (*En1* and *Wnt1*) responsible for scar deposition after wounding of dorsal skin and oral mucosa also address a long-standing question: Where do the dermal fibroblasts that deposit scar tissue after wounding come from? In the internal organs, some have shown that wound fibroblasts are derived from circulating fibroblast-like cells (30, 31) and that dermal architectures may be additionally supported by

nonmesenchyme lineages (32), as in kidney fibrosis. Our data indicate that within cutaneous tissues, a distinct and local lineage of resident fibroblasts is responsible for the fibrosis seen during wound healing, with an absence of ECM contributions from other mesenchyme or nonmesenchyme lineages. Our data also indicate that local fibroblasts, not circulating cells, are responsible for the connective tissue seen in the fibrosis formed in response to both radiation and carcinoma.

Targeting the fibroblast culprit behind cutaneous scarring

On the basis of CD26/DPP4 expression, we have prospectively isolated the lineage of cells that is responsible for the bulk of fibrosis, including the cells involved in tumor stroma. Our mouse data are consistent with reports on expression of CD26/DPP4 and its related serine protease FAPα (fibroblast activation protein-α) on stromal subsets of human cancers (33, 34). Depletions of FAPα-expressing stromal subsets from human cancers were recently shown to inhibit antitumor immunity and suppress tumor growth (34), and a similar anti-immunogenic mechanism could, in part, explain the CD26 depletion phenotypes of our tumor growth assays and slower rate of healing in wound-healing models.

Driskell *et al.* (27) have recently reported CD26 to be a marker of the upper dermis during fetal development. Our data demonstrate that CD26 is expressed in both upper and lower dermis at adult stages of development (Fig. 6B). The Driskell *et al.* report initially employs Pdgfrα-GFP transgenic mice (using FACS isolation of Pdgfra surface expression) to verify and prospectively isolate dermal fibroblasts from the backskin. Yet, our flow cytometry analysis on adult dermis indicates that 35% and 87% of EPFs and ENFs, respectively, do not express Pdgfrα surface protein (fig. S4C). Therefore, a significant fraction of the dermal fibroblasts assessed in our study are in fact absent from the analysis of the Driskell *et al.* report.

Given that CD26/DPP4 inhibitors such as sitagliptin (Merck) and vildagliptin (Novartis) have been approved by the FDA for the treatment for type 2 diabetes (35), it is possible that blood concentrations of orally administered gliptins may be sufficient to affect wound healing and fibrosis in patients. If not, clinical trials to test topical delivery of a CD26/DPP4 inhibitor in a dermal hydrogel or other local carrier would be an appropriate next step toward clinical implementation.

Materials and Methods

Mice

Mice were bred and maintained at the Stanford University Research Animal Facility in accordance with Stanford University guidelines. All the animals were housed in sterile micro-insulators and given water and rodent chow ad libitum. *En1*^{Cre}, *Wnt1*^{Cre}, *Sox9*^{Cre}, *Tie2*^{Cre}, *K5*^{Cre}, *K14*^{Cre}, *RAG-2*$^{-/-}$, *FVB*, *R26*$^{tm1(HBEGF)Awai}$, and *CAG-luc-eGFP L2G85* strains were obtained from Jackson laboratories. The *ROSA26*^{mTmG} (*R26*^{mTmG}) reporter mice, which harbor a double-fluorescent reporter that permanently replaces the expression of membrane-bound tomato red fluorescent protein (RFP) with membrane-bound GFP after recombination (10), were a gift from L. Luo (Stanford University). *En1*^{Cre} transgenic mice

were crossed with *R26*^{mTmG} reporter mice (Fig. 1A). *En1*^{Cre};*R26*^{mTmG} offspring were used to trace *En1*-lineage–positive fibroblasts (EPFs), defined in vivo by their GFP positivity, into the dorsal dermis.

Harvesting dermal fibroblasts

Mice were killed, and the dorsal fur was clipped; a hair-removal product was then applied topically to the dorsum for 1 to 5 min, followed by rinsing of the shaved skin with PBS. To preserve cell viability (36), dorsal skin was harvested immediately using dissecting scissors by separation along fascial planes and rinsed in betadine followed by 5x PBS washes on ice. Subcutaneous fat was then trimmed and cleaned from the dermis using a scalpel. Tissue was then incubated in 0.12 mg/mL Elastase (Abcam) in Dulbecco's modified Eagle's medium (DMEM) at 37°C for 25 min to allow for dermal-epidermal separation. Epidermis was then discarded, and dermis was mechanically diced with razor blades and dissecting scissors until samples reached uniform consistency. Oral mucosa was harvested using 3-mm biopsy punches and dissecting scissors along the buccal mucosa bilaterally and then processed identically to dorsal skin from this stage onward. After mechanical dissociation, samples were incubated in 20 mL Collagenase IV (Gibco) at a concentration of 4 mg/mL in DMEM [no fetal bovine serum (FBS)] on a water-bath shaker at 37°C for 1 hour. Samples were then passed through a 10-mL syringe (no needle) 5x and then through an 18.5 gauge syringe 5x, using “back loading” to load the syringe. Samples were placed back onto the shaker at 37°C for 1 hour. Enzymatic digestion was stopped by addition of 10% FBS DMEM, at which time the sample was centrifuged at 1250 revolutions per minute (rpm) for 5 min at 4°C to pellet cells. Supernatant was removed, with care taken to first remove the top layer of adipocytes before the remaining supernatant. Cells were resuspended in 10% FBS DMEM and passed through a 100-μm filter using centrifugation. The filtered suspension was further centrifuged at 1250 rpm for 5 min at 4°C. The supernatant was removed and the pellet was resuspended in 10% FBS DMEM and passed through a 70-μm filter. The filtered suspension was centrifuged again at 1250 rpm for 5 min, supernatant was removed, and the pellet was resuspended in ammonium-chloride-potassium (ACK) lysing buffer for 10 min at room temperature to facilitate lysis of red blood cells. ACK suspension was then diluted with equal volume FACS buffer and passed through a 40-μm filter. The filtered suspension was centrifuged at 1250 rpm for 5 min at 4°C, supernatant was removed, and the pellet was resuspended in FACS buffer containing deoxyribonuclease (DNase) (10 μg/ml). The cell suspension was then stained with PacBlue-conjugated CD31, CD45, Tie2, Ter119, and EpCAM for 20 min on ice and washed three times with FACS buffer and centrifuged. Cells were then resuspended in FACS buffer containing DNase(10 μg/ml) and 4′,6-diamidino-2-phenylindole (DAPI) (1X). FACS sorting (FACSAria III) for DAPI-negative, CD31-negative, CD45-negative, Tie2-negative, Ter119-negative, and EpCAM-negative cells (for hematopoietic, endothelial, and epithelial cells) was then performed to isolate dermal fibroblasts. Positivity for GFP or RFP allowed for the separation of EPFs from ENFs and WPFs from WNFs.

FACS analysis of dermal fibroblasts

All flow cytometry analysis on dermal fibroblasts described in this manuscript was performed on dissociated primary dermal fibroblasts after lineage-negative gating of

hematopoietic, endothelial, and epithelial cell lineages, using CD31, CD45, Tie2, Ter119, and EpCAM (CD326). The following antibodies were used to interrogate surface marker expression on EPFs and ENFs: CD44, CD73, CD90.1, CD90.2, CD105, biglycan, CD9, CD26, CD29, CD207, CD184, CD63, CD117, CD41, CD83, CD49e, CD49d, CD71, CD98, CD157, CD19, CD16/32, CD140a, CD172a, CD61, Ly-51, CD23, CD115, CD200, CD47, CD51, H2-Kb, and CD183 (BioLegend, eBioscience, Abcam). Cells were stained with a single anaphase-promoting complex conjugated antibody (above) during the harvest protocol along with PacBlue-conjugated CD31, CD45, Tie2, Ter119, and EpCAM antibodies. Cells were resuspended in FACS buffer and DAPI before FACS analysis.

Immunostaining of cultured fibroblasts

Fibroblasts (FACS-isolated as described previously from $En1^{Cre};R26^{mTmG}$ mice) were plated into 8-well culture slides for 2 days (BD Biosciences) and then fixed in 4% paraformaldehyde at 4°C for 10 min and stained with the following primary antibodies: FSP-1 (Abcam), vimentin (Abcam), α-SMA (Abcam), type IV collagen (Abcam), type III collagen (Abcam), type I collagen (Abcam), fibronectin (Abcam), and Thy1.1 (Abcam). Alexa Fluor 647–conjugated antirabbit, antigoat, or antirat antibodies (Invitrogen) were used as secondary and incubated for 1 hour. Fluorescent and bright-field images were taken with a Leica DM4000B microscope (Leica Microsystems) and RETIGA 2000R camera (QImaging Scientific Cameras).

Dorsal wounding

Four-week-old male $En1^{Cre};R26^{mTmG}$ and $R26^{mTmG}$ mice were used for cutaneous wound healing experiments. Both unsplinted and splinted excisional dorsal wounding was performed on $En1^{Cre};R26^{mTmG}$ and $R26^{mTmG}$ mice in accordance with well-established protocols. In brief, induction of anesthesia was performed under 2.5% isoflurane/oxygen mixture at 2 l per minute followed by maintenance anesthesia at 1 L per minute. Dorsal fur was clipped, hair-removal product was applied topically to dorsal skin for 1 to 5 min or until depilation was achieved, and skin was prepped with povidone-iodine and alcohol. Two 6-mm full-thickness circular wounds were placed through the panniculus carnosus on the dorsum of each animal at the same level, ~6 mm below the ears and 4 mm lateral to the midline. Unsplinted wounds were dressed with sterile Tegaderm (3M) at this stage. For splinted wounds, two circular silicone 12-mm diameter stents (Invitrogen) were placed around the perimeter of each wound and secured in place with glue and 8 simple interrupted Ethilon 6-0 sutures (Ethicon). Dressings were changed every other day under anesthesia until full wound closure.

Oral wounding

Four-week-old male $Wnt1^{Cre};R26^{mTmG}$ mice were used for oral wound healing experiments. In brief, mice were anesthetized with isoflurane/oxygen mixture as previously described. Full thickness wounds were excised on both sides of the buccal mucosa using a 1.5-mm biopsy punch. Wounds were harvested 14 days after surgery.

Melanoma transplantation

Depilation of the dorsal backs of 5-week-old male *En1*^{Cre};*R26*^{mTmG} mice was performed as described previously in the section “Dorsal wounding.” The B16-F10 mouse melanoma cell line (ATCC) was passaged twice in culture and injected inter-dermally into the dorsal skin of each mouse (5.0×10^4 cells per injection). After 30 days, a palpable tumor had formed and was harvested at that stage for histology.

Model of radiation-induced fibrosis (skin)

All irradiation was performed using a Kimtron Polaris SC-500 Series II x-ray machine (Kimtron, Inc., Oxford, Connecticut, USA; 225 kV, 13.3 mA, 0.5 mm Cu, 1 Gy/min) according to Stanford University Administrative Panel on Laboratory Animal Care (APLAC) protocol #9981. Mice were anesthetized with a 50% concentration (1:1 dilution with 0.9% NaCl) of anesthetic cocktail consisting of ketamine hydrochloride (80 mg/kg), xylazine (2.5 mg/kg), and acepromazine (2.5 mg/kg). The dorsal backs of mice were prepared by removing fur by clipping and light application of depilatory cream. Mice were placed onto customized individual lead jigs allowing dorsal cutaneous exposure to a circumferential region 2 cm in diameter. The dorsum of each mouse was irradiated with 2 doses of 40 Gy spaced 7 days apart. Mice were killed on day 14 after the first dose when signs of acute skin reactions (erythema and moist desquamation) were present.

Reciprocal transplantation into cutaneous and oral wounds

Dermal fibroblasts were harvested for FACS, as previously described, from the oral dermis of *Wnt1*^{Cre};*R26*^{mTmG} mice and the dorsal dermis of *En1*^{Cre};*R26*^{mTmG} mice at 4 weeks of age. Harvested cells were stained with DAPI, as well as PacBlue-conjugated CD31 (1:100), CD45 (1:200), and Ter-119 (1:200), and sorted for viable GFP$^+$/CD31$^-$/CD45$^-$/Ter-119$^-$ populations from each anatomical site. FACS-isolated cells from the dorsal dermis of *En1*^{Cre};*R26*^{mTmG} mice were transplanted into the buccal mucosa (described previously) of recipient *RAG-2*$^{-/-}$ double-knockout mice (1.0×10^5 cells per site). FACS-isolated cells from the oral dermis of *Wnt1*^{Cre};*R26*^{mTmG} mice were transplanted into the dorsal dermis of recipient *RAG-2*$^{-/-}$ double-knockout mice (1.0×10^5 cells per site). All tissues were harvested for analysis at 10 days after transplantation.

Histology and tissue analysis

For fixation, tissues were placed in 2% paraformaldehyde for 12 to 16 hours at 4°C. Samples were prepared for embedding by soaking in 30% sucrose in PBS at 4°C for 24 hours. Samples were removed from the sucrose solution, and tissue blocks were prepared by embedding in Tissue Tek O.C.T. (Sakura Finetek) under dry ice to freeze the samples within the compound. Frozen blocks were mounted on a MicroM HM550 cryostat (MICROM International GmbH), and 5- to 8-μm-thick sections were transferred to Superfrost/Plus adhesive slides (Fisher brand).

Immunohistochemistry

For hematoxylin and eosin staining and Masson's trichrome staining, standardized protocols were used with no modifications. Immunostaining on frozen sections was performed using

the following primary antibodies: type I collagen, type III collagen (Abcam), type IV collagen (Abcam), keratin-14 (Abcam), CD26 (eBioscience), CD29 (eBioscience), biglycan (Abcam), and FABP4 (Abcam). Briefly, slides were fixed in cold acetone (–20°C), and then blocked for 30 min in 10% bovine serum albumin with 5% horse serum followed by incubation with primary antibody for 12 to 16 hours. Slides were then incubated for 1 hour with Alexa Fluor 647–conjugated antirabbit, antigoat, or antirat secondary antibodies (Invitrogen). Fluorescent and bright-field images were taken with a Leica DM4000B microscope (Leica Microsystems) and RETIGA 2000R camera (QImaging Scientific Cameras).

TUNEL staining

Terminal deoxynucleotidyl transferase–mediated deoxyuridine triphosphate nick end labeling (TUNEL) staining was performed using DeadEnd Fluorometric TUNEL System (Promega, Madison, Wisconsin) according to the manufacturer's protocol. Analysis was performed by counting positive cells per high-power field.

Micoarray analysis

Dermal fibroblasts were harvested for FACS from the oral dermis and cranial dermis of $Wnt1^{Cre};R26^{mTmG}$ mice and from ventral and dorsal dermis of $En1^{Cre};R26^{mTmG}$ mice, as previously described. For all microarray analysis, EPFs and ENFs where harvested from backskin of adult (P56) mice. Positivity for GFP or RFP allowed for the separation of EPFs from ENFs and WPFs from WNFs. RNA was precipitated via chloroform-phenol extraction. Samples were processed for cleanup and concentration using RNeasy MinElute cleanup kit (cat. 74204, QIAGEN). RNA yield was typically 0.5 to 1 μg RNA/sorted subpopulations. RNA samples from all sorted populations were converted to cDNA using SuperScript III first-strand synthesis system for RT-PCR (cat. 18080-051, Invitrogen) and hybridized to Affymetrix Mouse Genome 430 2.0 arrays. Microarrays were normalized by robust multichip average and quantile normalization in R. Cluster analysis was performed with AutoSOME (22), using the following settings for gene expression clustering: *P*-value threshold of 0.05, 100 ensemble iterations, unit variance normalization of arrays, median centering of genes, and sum of squares = 1 normalization for both genes and arrays. The following settings were used for AutoSOME fuzzy clustering: *P*-value threshold of 0.05, 500 ensemble iterations, unit variance normalization of arrays, and uncentered correlation for distance matrix construction. The fuzzy cluster network (Fig. 3F) was rendered with Cytoscape 2.8.3 (37).

Cell surface marker screening

Dermal fibroblasts were harvested as described previously from adult (P56) $En1^{Cre};R26^{mTmG}$ transgenic mice. Cells were analyzed using BD Lyoplate Mouse Cell Surface Marker Screening Panel (BD Biosciences, cat. 562208) containing 176 purified monoclonal antibodies and corresponding isotype controls. Manufacturer's staining protocol was followed with slight modifications. Cells isolated from the dorsal dermis of $En1^{Cre};R26^{mTmG}$ mice were plated into U-bottom 96-well plates at a density of 2.5 to 5×10^5 cells per well in FACS buffer. Primary antibody incubation was done in 100-μl volume for 30 min on ice. Next, cells were incubated with biotinylated secondary antibodies (goat

antimouse 1:400, goat antirat 1:400, goat antisyrian hamster 1:400, goat anti–Armenian hamster 1:800) in 100-μl volume for 30 min on ice. Tertiary incubation with Alexa Fluor 647 Streptavidin (1:4000)—as well as PacBlue-conjugated CD31 (1:100), CD45 (1:200)—and Ter-119 (1:200), was carried out in 100-μl volume for 30 min on ice. Analysis was performed using flow cytometer BD LSR Fortessa with High Throughput Sampler.

Intradermal transplantation of CD26$^+$ and CD26$^-$ fibroblasts

$CD26^+Lin^-$ and $CD26^-Lin^-$ dermal fibroblasts from the dorsal skin of uncrossed $R26^{mTmG}$ mice (at 6 to 8 weeks of age) were harvested as previously described, and 2.0×10^5 cells from each of these populations were transplanted via intradermal injection (in 100 μl PBS) into the dorsal backs of $RAG\text{-}2^{-/-}$ double-knockout mice. Grafts containing FACS-sorted cells alone were harvested after 10 days and processed for histology.

Intradermal cotransplantation of CD26$^+$ and CD26$^-$ fibroblasts with B16 mouse melanoma

$CD26^+Lin^-$ and $CD26^-Lin^-$ dermal fibroblasts from the dorsal skin of uncrossed $R26^{mTmG}$ mice (at 6 to 8 weeks of age) were harvested, as previously described, and 2.0×10^5 cells from each of these populations were cotransplanted intradermally along with 5.0×10^4 B16-F10 mouse melanoma cells (ATCC) into the dorsal backs of $RAG\text{-}2^{-/-}$ double-knockout mice. Grafts were harvested 30 days after transplantation and processed for histology.

Fluorescence quantification

Randomly chosen sections ($n = 25$) from both $CD26^+Lin^-$ and $CD26^-Lin^-$ intradermal fibroblast grafts and melanoma cotransplant grafts were analyzed using ImageJ software. The “mean gray value” (sum of the gray values of all the pixels in the selection divided by the number of pixels) for the entire image was calculated for images taken in the RFP channel only. The mean gray value measuring total RFP signal for a given image was then normalized to the number of RFP-positive cells in that image. All data are quantified by a blinded observer from digital photographs analyzed using ImageJ and Adobe Photoshop CS6 (Adobe Systems, San Jose, California).

qRT-PCR analysis of CD26$^+$ and CD26$^-$ fibroblasts transplanted into dorsal wounds

$CD26^+$ ($n = 3$) and $CD26^-$ ($n = 3$) grafts were harvested at 7 days after transplant (10 days after wounding), digested using Liberase (1 mg/mL in DMEM). Cells harvested from each graft were then FACS-sorted for viability (DAPI) and RFP positivity directly into TRIZOL. Reverse transcription was performed with 1 ug RNA using Taqman Reverse Transcription Reagents (Applied Biosystems), and qRT-PCR was carried out using Applied Biosystems Prism 7900HT Sequence Detection System and SYBR Green PCR Master Mix (Applied Biosystems). Expression of collagen type I and alpha-smooth muscle actin (alpha-SMA) mRNA was measured. mRNA amounts were calculated relative to the amount of β-actin mRNA in the same samples. For primers, see table S1.

qRT-PCR analysis of Cre expression

Fibroblasts were FACS-isolated using the fibroblast isolation methodology discussed previously from the dorsal skin of P1 $R26^{mTmG}$ ($n = 3$) skin, E11.5 $En1^{Cre}$ ($n = 3$) skin,

$R26^{mTmG}$ ($n = 3$) skin, P1 $En1^{Cre};R26^{mTmG}$ ($n = 3$) skin, P30 $En1^{Cre};R26^{mTmG}$ ($n = 3$) skin, and dorsal wounds on P30 $En1^{Cre};R26^{mTmG}$ ($n = 3$) mice. Fibroblasts were sorted directly into TRIZOL. Reverse transcription was performed with 1 ug RNA using Taqman Reverse Transcription Reagents (Applied Biosystems), and qRT-PCR was carried out using Applied Biosystems Prism 7900HT Sequence Detection System and SYBR Green PCR Master Mix (Applied Biosystems). mRNA amounts were calculated relative to the amount of β-actin mRNA in the same samples. For primers, see table S1.

Microfluidic single-cell gene expression analysis

Gene lists defining fibroblast and nonfibroblast markers were collected from a literature search (38, 39). Single-cell reverse transcription and low cycle pre-amplification were performed as previously described (24, 40). Briefly, dermal lysate cell suspensions were sorted from $En1^{Cre};R26^{mTmG}$ transgenic mice (at 6 to 8 weeks of age) as single cells into each well of a 96-well plate using a Becton Dickinson FACS Aria flow cytometer (Franklin Lakes, NJ) into 6 μl of lysis buffer and SUPERase-In RNAse inhibitor (Applied Biosystems, Foster City, CA) ($n = 6$ cell lines). Live/dead gating was performed based on DAPI exclusion. EPFs and ENFs were defined as previously described. Live, single cells were also sorted as unfractionated dermis. Reverse transcription and low-cycle pre-amplification were performed using Cells Direct (Invitrogen) with Taqman assay primer sets (Applied Biosystems) as per the manufacturer's specifications. Exon-spanning primers were used where possible to avoid amplification of genomic background. cDNA was loaded onto 96.96 Dynamic Arrays (Fluidigm, South San Francisco, California) for qPCR amplification using Universal PCR Master Mix (Applied Biosystems) with a uniquely compiled Taqman assay primer set (table S1), as previously described (41).

Statistical analysis of single-cell data

Analysis of single-cell data was performed, as described previously (42). Briefly, data from all samples were normalized relative to the pooled median expression for each gene and converted to base 2 logarithms. Absolute bounds (±5 cycle thresholds from the median or 32-fold increases/decreases in expression) were set, and nonexpressers were assigned to this floor. Clustergrams were then generated using hierarchical clustering (with a “complete” linkage function and Euclidean distance metric) to facilitate data visualization (MATLAB R2011b, MathWorks, Natick, Massachusetts).

To detect overlapping patterns within the single-cell transcriptional data, *k*-means clustering was employed using a standard Euclidean distance metric. Accordingly, each cell was assigned membership to a specific cluster as dictated by similarities in expression profiles (minimizing the within-cluster sum of square distances) in MATLAB. Optimally partitioned clusters were then subgrouped using hierarchical clustering to facilitate visualization of data patterning (41, 42). Nonparametric, two-sample Kolmogorov-Smirnov (K-S) tests were used to identify those genes with expression patterns that differed significantly between population clusters and/or groups, following Bonferroni correction for multiple samples using a strict cutoff of $P < 0.05$. For subgroup comparisons, the empirical distribution of cells from each cluster was evaluated against that of the remaining cells in the experiment. Ingenuity Pathway Analysis (IPA, Ingenuity Systems, Redwood City, California) was used

to construct transcriptome networks based on genes that were significantly increased within clusters (including both direct and indirect relationships).

Small molecule-based CD26 inhibition during wound healing using diprotin A

Background strain (*B6*) mice aged 4 to 6 weeks were dorsally wounded, and pullulan-collagen scaffolds seeded with either 500 ng diprotin A + carrier or carrier alone were loaded onto the wound site at the time of wounding. On days 3 and 6 after wounding, new scaffolds seeded as on day 0 were loaded onto the wound site. Wound healing was then allowed to proceed unperturbed until completion. Photographic images taken every 2 or 3 days documented wound and scar size until healing reached completion.

DTR-based ablation of EPFs (GFP^{+}) during cutaneous wounding

$En1^{Cre};R26^{mTmG};R26^{tm1(HBEGF)Awai}$ mice were dorsally wounded (splinted 6 mm excisional) and pullulan-collagen dermal hydrogels seeded with either 200 ng DT in PBS or PBS alone (control) were transplanted onto the wound sites at the time of wounding (day 0). On days 3 and 6 after wounding, new hydrogels seeded as on day 0 were transplanted onto the wound sites. Photographic images taken every 2 days documented wound and scar size until healing reached completion, at which point wounds were harvested for histologic analysis of GFP/RFP fluorescence and connective tissue deposition by Maisson's trichrome.

Quantification of scar size

Gross scar size is determined by quantifying the area of the scar relative to the inner ring of the silicone splint on the day all wounds have completely healed. Scar size is represented as a percentage of the original wound at baseline (day 0). All data are quantified by a blinded observer from digital photographs analyzed using Adobe Photoshop CS6 (Adobe Systems, San Jose, California).

Quantification of the rate of wound healing

Rate of wound healing is determined by quantifying the area of the wound relative to the inner ring of the silicone splint at baseline (day 0), 3 days after each application of hydrogel, and every 2 days. Wound size is then calculated as a percent of the original wound at baseline. All data are quantified by a blinded observer from digital photographs analyzed using Adobe Photoshop CS6 (Adobe Systems).

Tensile strength testing

Tensile strength tests for fully healed wounds on $En1^{Cre};R26^{mTmG};R26^{tm1(HBEGF)Awai}$ mice treated with or without DT via pullulan-collagen hydrogel on days 0, 3, and 6 was performed on day 22 and day 16, respectively. Tests were performed with a microtester (model 5848, Instron, Norwood, Massachusetts) equipped with a 100 N load cell. The tissue specimens were attached to custom grips with double-sided tape, giving a final gauge length of 10 mm. The region between the grips (gauge region) was stretched until a break in the skin was detected by a decrease in stress with increasing strain. Analysis was performed as previously described (43). True strain was calculated as the change in length divided by the gauge length, and true stress was calculated as the force divided by the original cross-

sectional area. The tensile strength was determined as the greatest true stress achieved. The modulus was determined via least squares regression as the slope of the linear region of the true stress-true strain curve ($R^2 \geq 0.99$).

DTR-based ablation of EPFs (GFP$^+$) before melanoma transplantation

En1^{Cre};*R26*^{mTmG};*R26*$^{tm1(HBEGF)Awai}$ mice were injected (4x) intradermally with either 100 ng DT in 25 ul PBS ($n = 7$) or 25 ul PBS alone ($n = 7$) in four evenly spaced locations along the circumference, 6 mm in diameter. Twenty-four hours later, 5.0×10^5 B16 mouse melanoma cells were transplanted intradermally into the middle of the marked circle on the dorsum of these mice. Tumors were allowed to grow in DT-treated ($n = 7$) and control mice ($n = 7$) until killing was dictated by protocol parameters (tumor size >2 cm) for one mouse, at which point all mice were killed and tumors were harvested for analysis.

Supplementary Material

Refer to Web version on PubMed Central for supplementary material.

ACKNOWLEDGMENTS

We thank D. T. Montoro and S. D. Morrison for their early contribution to developing the live fibroblast harvest protocol. This work was supported in part by NIH grant R01 GM087609 (to H.P.L.), a gift from Ingrid Lai and Bill Shu in honor of Anthony Shu (to H.P.L.), the California Institute of Regenerative Medicine (RC1 00354 to I.L.W.), the Smith Family Trust (to I.L.W.), the Hagey Laboratory for Pediatric Regenerative Medicine and The Oak Foundation (to M.T.L., H.P.L., and G.C.G.), NIH grants U01 HL099776 (to M.T.L.) and U01 HL099999 (to I.L.W.), the Virginia and D. K. Ludwig Fund for Cancer Research (to I.L.W.), and the Gunn/Olivier fund (to M.T.L. and I.L.W.). G.G.W. was supported by the Stanford School of Medicine, the Stanford Medical Scientist Training Program, and National Institute of General Medical Sciences training grant GM07365. Y.R. was supported by the Human Frontier Science Program (HFSP) Long Term Fellowship, the Machiah Foundation Fellowship, and the Siebel Scholarship. M.S.H. was supported by the California Institute for Regenerative Medicine Clinical Fellow training grant TG2-01159. Z.N.M. was supported by the Plastic Surgery Foundation Research Fellowship grant 114288 and the Translational Research and Applied Medicine program pilot grant. Microarray data are available at the Gene Expression Omnibus (GEO) at www.ncbi.nlm.nih.gov/geo, under accession number GSE65402.

REFERENCES AND NOTES

1. Sorrell JM, Caplan AI. Fibroblasts-a diverse population at the center of it all. Int. Rev. Cell Mol. Biol. 2009; 276:161–214. doi: 10.1016/S1937-6448(09)76004-6; pmid: 19584013. [PubMed: 19584013]
2. Wynn TA. Cellular and molecular mechanisms of fibrosis. J. Pathol. 2008; 214:199–210. doi: 10.1002/path.2277; pmid: 18161745. [PubMed: 18161745]
3. Powell DW, et al. Myofibroblasts. I. Paracrine cells important in health and disease. Am. J. Physiol. 1999; 277:C1–C9. doi: 10.1111/j.1469-7793.1999.001af.x; pmid: 10409103. [PubMed: 10409103]
4. Wilson MS, Wynn TA. Pulmonary fibrosis: Pathogenesis, etiology and regulation. Mucosal Immunol. 2009; 2:103–121. doi: 10.1038/mi.2008.85; pmid: 19129758. [PubMed: 19129758]
5. Hinz B, et al. The myofibroblast: One function, multiple origins. Am. J. Pathol. 2007; 170:1807–1816. doi: 10.2353/ ajpath.2007.070112; pmid: 17525249. [PubMed: 17525249]
6. Dumont N, et al. Breast fibroblasts modulate early dissemination, tumorigenesis, and metastasis through alteration of extracellular matrix characteristics. Neoplasia. 2013; 15:249–262. pmid: 23479504. [PubMed: 23479504]
7. Servais C, Erez N. From sentinel cells to inflammatory culprits: Cancer-associated fibroblasts in tumour-related inflammation. J. Pathol. 2013; 229:198–207. doi: 10.1002/path.4103; pmid: 22996812. [PubMed: 22996812]

8. Tripathi M, Billet S, Bhowmick NA. Understanding the role of stromal fibroblasts in cancer progression. Cell Adhes. Migr. 2012; 6:231–235. doi: 10.4161/cam.20419; pmid: 22568983.
9. Orimo A, Weinberg RA. Stromal fibroblasts in cancer: A novel tumor-promoting cell type. Cell Cycle. 2006; 5:1597–1601. doi: 10.4161/cc.5.15.3112; pmid: 16880743. [PubMed: 16880743]
10. Muzumdar MD, Tasic B, Miyamichi K, Li L, Luo L. A global double-fluorescent Cre reporter mouse. Genesis. 2007; 45:593–605. doi: 10.1002/dvg.20335; pmid: 17868096. [PubMed: 17868096]
11. Atit R, et al. Beta-catenin activation is necessary and sufficient to specify the dorsal dermal fate in the mouse. Dev. Biol. 2006; 296:164–176. doi: 10.1016/j.ydbio.2006.04.449; pmid: 16730693. [PubMed: 16730693]
12. Weber L, Kirsch E, Müller P, Krieg T. Collagen type distribution and macromolecular organization of connective tissue in different layers of human skin. J. Invest. Dermatol. 1984; 82:156–160. doi: 10.1111/1523-1747.ep12259720; pmid: 6693779. [PubMed: 6693779]
13. Cao YA, et al. Shifting foci of hematopoiesis during reconstitution from single stem cells. Proc. Natl. Acad. Sci. U.S.A. 2004; 101:221–226. doi: 10.1073/pnas.2637010100; pmid: 14688412. [PubMed: 14688412]
14. Gottlöber P, et al. Interferon-gamma in 5 patients with cutaneous radiation syndrome after radiation therapy. Int. J. Radiat. Oncol. Biol. Phys. 2001; 50:159–166. doi: 10.1016/S0360-3016(00)01542-X; pmid: 11316559. [PubMed: 11316559]
15. Labrousse AL, Ntayi C, Hornebeck W, Bernard P. Stromal reaction in cutaneous melanoma. Crit. Rev. Oncol. Hematol. 2004; 49:269–275. doi: 10.1016/j.critrevonc.2003.10.007; pmid: 15036266. [PubMed: 15036266]
16. Moore K, Moore M. Intra-tumour host cells of transplanted rat neoplasms of different immunogenicity. Int. J. Cancer. 1977; 19:803–813. doi: 10.1002/ijc.2910190610; pmid: 326682. [PubMed: 326682]
17. Udagawa T, Puder M, Wood M, Schaefer BC, D'Amato RJ. Analysis of tumor-associated stromal cells using SCID GFP transgenic mice: Contribution of local and bone marrow-derived host cells. FASEB J. 2006; 20:95–102. doi: 10.1096/fj.04-3669com; pmid: 16394272. [PubMed: 16394272]
18. Szpaderska AM, Zuckerman JD, DiPietro LA. Differential injury responses in oral mucosal and cutaneous wounds. J. Dent. Res. 2003; 82:621–626. doi: 10.1177/154405910308200810; pmid: 12885847. [PubMed: 12885847]
19. Janebodin K, et al. Isolation and characterization of neural crest-derived stem cells from dental pulp of neonatal mice. PLOS ONE. 2011; 6:e27526. doi: 10.1371/journal. pone.0027526; pmid: 22087335. [PubMed: 22087335]
20. Nichols DH, Bruce LL. Migratory routes and fates of cells transcribing the Wnt-1 gene in the murine hindbrain. Dev. Dyn. 2006; 235:285–300. doi: 10.1002/dvdy.20611; pmid: 16273520. [PubMed: 16273520]
21. Yoshida T, Vivatbutsiri P, Morriss-Kay G, Saga Y, Iseki S. Cell lineage in mammalian craniofacial mesenchyme. Mech. Dev. 2008; 125:797–808. doi: 10.1016/j.mod.2008.06.007; pmid: 18617001. [PubMed: 18617001]
22. Newman AM, Cooper JB. AutoSOME: A clustering method for identifying gene expression modules without prior knowledge of cluster number. BMC Bioinformatics. 2010; 11:117. doi: 10.1186/1471-2105-11-117; pmid: 20202218. [PubMed: 20202218]
23. Hansen LS, Coggle JE, Wells J, Charles MW. The influence of the hair cycle on the thickness of mouse skin. Anat. Rec. 1984; 210:569–573. doi: 10.1002/ar.1092100404; pmid: 6524697. [PubMed: 6524697]
24. Galiano RD, Michaels J 5th, Dobryansky M, Levine JP, Gurtner GC. Quantitative and reproducible murine model of excisional wound healing. Wound Repair Regen. 2004; 12:485–492. doi: 10.1111/j.1067-1927.2004.12404.x; pmid: 15260814. [PubMed: 15260814]
25. Nielsen JS, McNagny KM. Novel functions of the CD34 family. J. Cell Sci. 2008; 121:3683–3692. doi: 10.1242/jcs.037507; pmid: 18987355. [PubMed: 18987355]
26. Willingham SB, et al. The CD47-signal regulatory protein alpha (SIRPa) interaction is a therapeutic target for human solid tumors. Proc. Natl. Acad. Sci. U.S.A. 2012; 109:6662–6667. doi: 10.1073/pnas.1121623109; pmid: 22451913. [PubMed: 22451913]

27. Driskell RR, et al. Distinct fibroblast lineages determine dermal architecture in skin development and repair. Nature. 2013; 504:277–281. doi: 10.1038/nature12783; pmid: 24336287. [PubMed: 24336287]
28. Arwert EN, et al. Upregulation of CD26 expression in epithelial cells and stromal cells during wound-induced skin tumour formation. Oncogene. 2012; 31:992–1000. doi: 10.1038/onc.2011.298; pmid: 21765471. [PubMed: 21765471]
29. Hiramatsu H, et al. The crystal structure of human dipeptidyl peptidase IV (DPPIV) complex with diprotin A. Biol. Chem. 2004; 385:561–564. doi: 10.1515/BC.2004.068; pmid: 15255191. [PubMed: 15255191]
30. Quan TE, Cowper S, Wu SP, Bockenstedt LK, Bucala R. Circulating fibrocytes: Collagen-secreting cells of the peripheral blood. Int. J. Biochem. Cell Biol. 2004; 36:598–606. doi: 10.1016/j.biocel.2003.10.005; pmid: 15010326. [PubMed: 15010326]
31. Schmidt M, Sun G, Stacey MA, Mori L, Mattoli S. Identification of circulating fibrocytes as precursors of bronchial myofibroblasts in asthma. J. Immunol. 2003; 171:380–389. doi: 10.4049/jimmunol.171.1.380; pmid: 12817021. [PubMed: 12817021]
32. LeBleu VS, et al. Origin and function of myofibroblasts in kidney fibrosis. Nat. Med. 2013; 19:1047–1053. doi: 10.1038/nm.3218; pmid: 23817022. [PubMed: 23817022]
33. Atherton AJ, et al. Dipeptidyl peptidase IV expression identifies a functional sub-population of breast fibroblasts. Int. J. Cancer. 1992; 50:15–19. doi: 10.1002/ijc.2910500105; pmid: 1345821. [PubMed: 1345821]
34. Kraman M, et al. Suppression of antitumor immunity by stromal cells expressing fibroblast activation protein-alpha. Science. 2010; 330:827–830. doi: 10.1126/science.1195300; pmid: 21051638. [PubMed: 21051638]
35. Ahrén B. DPP-4 inhibitors. Best Pract. Res. Clin. Endocrinol. Metab. 2007; 21:517–533. doi: 10.1016/j.beem.2007.07.005; pmid: 18054733. [PubMed: 18054733]
36. Parrinello S, et al. Oxygen sensitivity severely limits the replicative lifespan of murine fibroblasts. Nat. Cell Biol. 2003; 5:741–747. doi: 10.1038/ncb1024; pmid: 12855956. [PubMed: 12855956]
37. Shannon P, et al. Cytoscape: A software environment for integrated models of biomolecular interaction networks. Genome Res. 2003; 13:2498–2504. doi: 10.1101/gr.1239303; pmid: 14597658. [PubMed: 14597658]
38. Rendl M, Lewis L, Fuchs E. Molecular dissection of mesenchymal-epithelial interactions in the hair follicle. PLOS Biol. 2005; 3:e331. doi: 10.1371/journal.pbio.0030331; pmid: 16162033. [PubMed: 16162033]
39. Joe AW, et al. Muscle injury activates resident fibro/adipogenic progenitors that facilitate myogenesis. Nat. Cell Biol. 2010; 12:153–163. doi: 10.1038/ncb2015; pmid: 20081841. [PubMed: 20081841]
40. Levi B, et al. CD105 protein depletion enhances human adipose-derived stromal cell osteogenesis through reduction of transforming growth factor b1 (TGF-b1) signaling. J. Biol. Chem. 2011; 286:39497–39509. doi: 10.1074/jbc.M111.256529; pmid: 21949130. [PubMed: 21949130]
41. Januszyk M, et al. Diabetes irreversibly depletes bone marrow-derived mesenchymal progenitor cell subpopulations. Diabetes. 2014; 63:3047–3056. doi: 10.2337/db13-1366; pmid: 24740572. [PubMed: 24740572]
42. Glotzbach JP, et al. An information theoretic, microfluidic-based single cell analysis permits identification of subpopulations among putatively homogeneous stem cells. PLOS ONE. 2011; 6:e21211. doi: 10.1371/journal.pone.0021211; pmid: 21731674. [PubMed: 21731674]
43. Rustad KC, et al. Enhancement of mesenchymal stem cell angiogenic capacity and stemness by a biomimetic hydrogel scaffold. Biomaterials. 2012; 33:80–90. doi: 10.1016/j. biomaterials.2011.09.041; pmid: 21963148. [PubMed: 21963148]

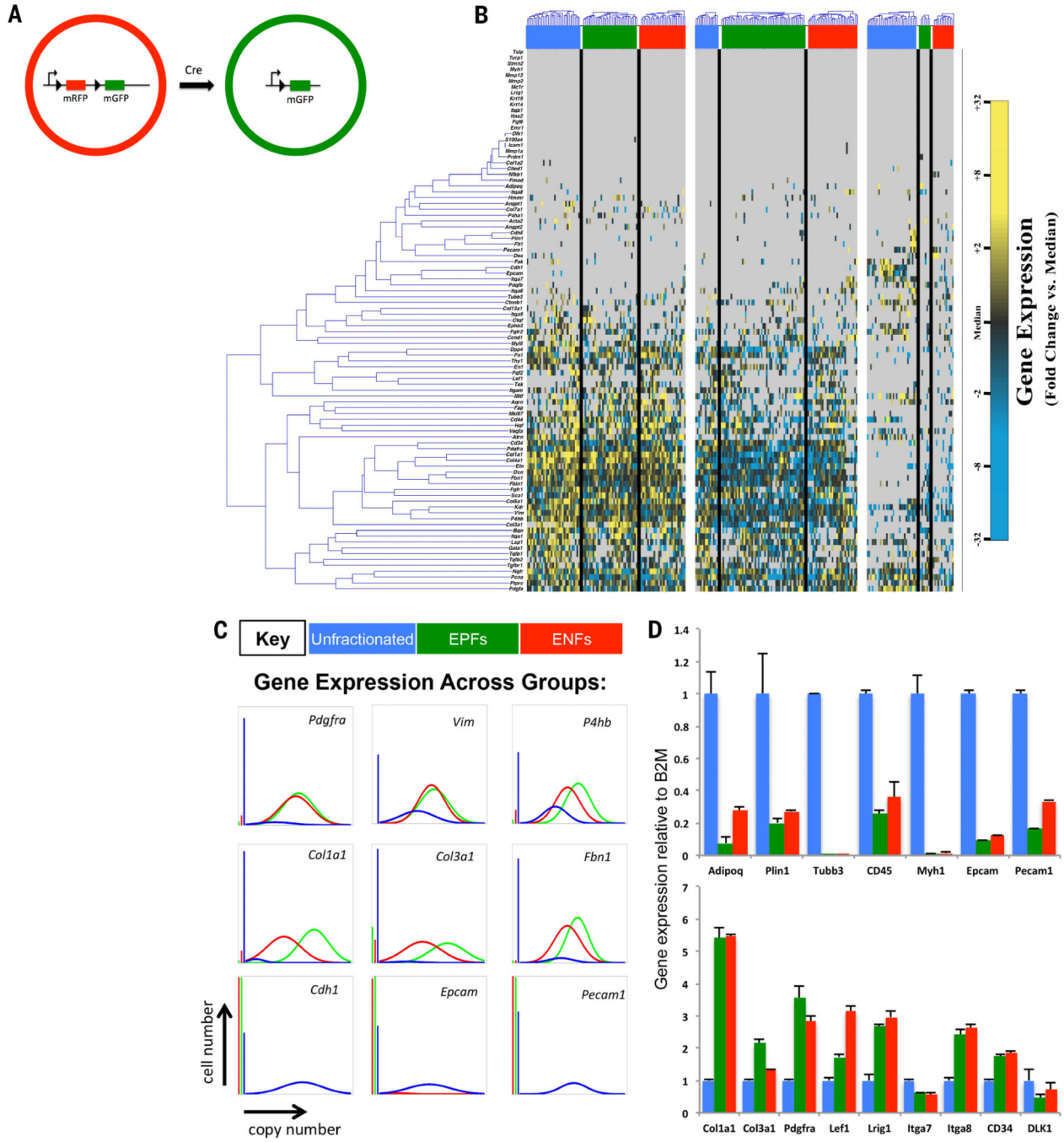

Fig. 1. Gene expression analysis of EPFs and ENFs

(**A**) Schematic showing mTmG system. (**B**) Hierarchical clustering of simultaneous gene expression for at least 70 individual cells FACS-isolated as either unfractionated dermal lysate (blue), EPFs (green), or ENFs (red) in P56 $En1^{Cre};R26^{mTmG}$ mice. Gene expression is presented as relative (fold) change from median on a color scale from yellow (high expression, 32-fold above median) to blue (low expression, 32-fold below median). *K*-means clustering of cells demonstrates two “fibroblast” clusters and a smaller nonfibroblast population. (**C**) Differentially expressed genes between unfractionated dermal lysate cells,

EPFs, and ENFs identified using nonparametric two-sample Kolmogorov-Smirnov testing ($P < 0.01$ after Bonferroni correction for multiple comparisons). Distributions of single-cell gene expression between populations are illustrated here using median-centered Gaussian curve fits. The left bar for each panel represents the fraction of qPCR reactions that failed to amplify in each group. (**D**) qRT-PCR analysis of fibroblast- and nonfibroblast-associated gene expression in unfractionated dermal lysate and FACS-isolated EPFs and ENFs.

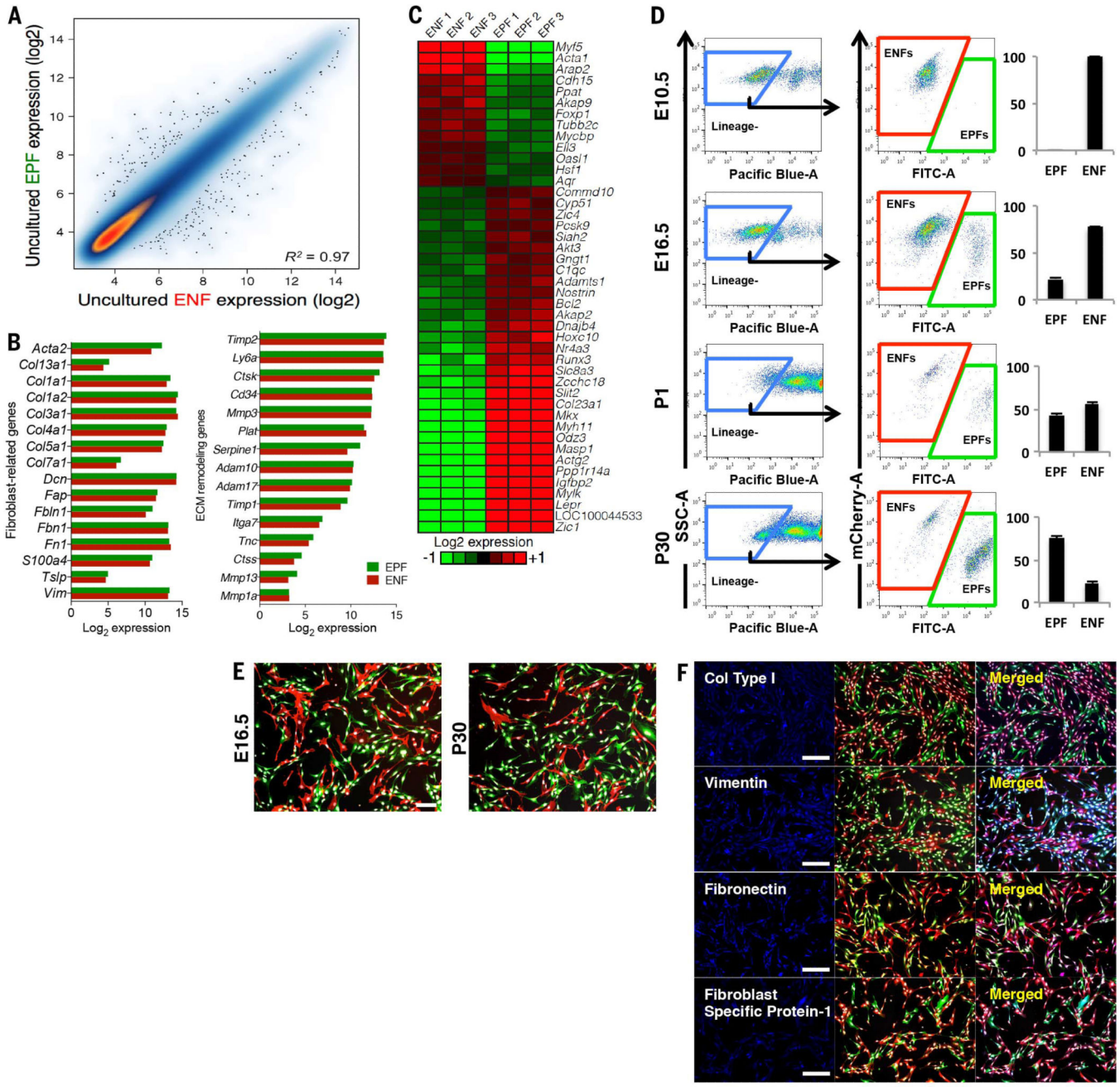

Fig. 2. EPFs and ENFs are two distinct lineages of fibroblasts

(**A**) Scatter plot depicting transcriptome-wide expression differences between uncultured FACS-isolated EPF and ENF populations from P56 *En1*^{Cre};*R26*^{mTmG} mice. For each population (n = 3), the median expression of each gene is plotted. Within the scatter plot, gene density is represented as a heat map, with orange regions containing larger numbers of genes than blue regions. Outliers are shown as individual points. (**B**) Similar expression of known fibroblast markers and fibroblast-related genes (left) and ECM remodeling genes (right) compared between uncultured FACS-isolated EPF and ENF populations by microarray analysis. (**C**) Expression of top differentially regulated genes between uncultured

FACS-isolated EPF and ENF populations by microarray analysis. Genes were filtered for *Q* value of <0.3 (30% false discovery rate) and a fold change of at least 1.5x. (**D**) FACS analysis showing abundance of EPFs and ENFs FACS-isolated from the dorsal dermis of E10.5 (top), E16.5 (one down from top), P1 (one up from bottom), and P30 (bottom) $En1^{Cre};R26^{mTmG}$ mice reveals a shift in population dynamics during dermal development from ENF-dominated dermis at E10.5 to EPF-dominated dermis at P1 and subsequent postnatal stages ($n = 5$ mice). (**E**) Fluorescent imaging of EPFs and ENFs cultured after FACS-sorting from the dorsal dermis of E16.5 and P30 $En1^{Cre};R26^{mTmG}$ mice. The relative abundance of EPFs and ENFs defined in the FACS analyses was consistent with the relative abundance seen after tissue culture plating at each time point. Scale bar, 100 μm. (**F**) Immunostaining of FACS-isolated EPFs and ENFs from P30 $En1^{Cre};R26^{mTmG}$ mice in vitro revealed that traditional fibroblast markers (vimentin and FSP-1) and secreted ECM components (col type I and fibronectin) are expressed similarly across both populations. Scale bar, 200 μm.

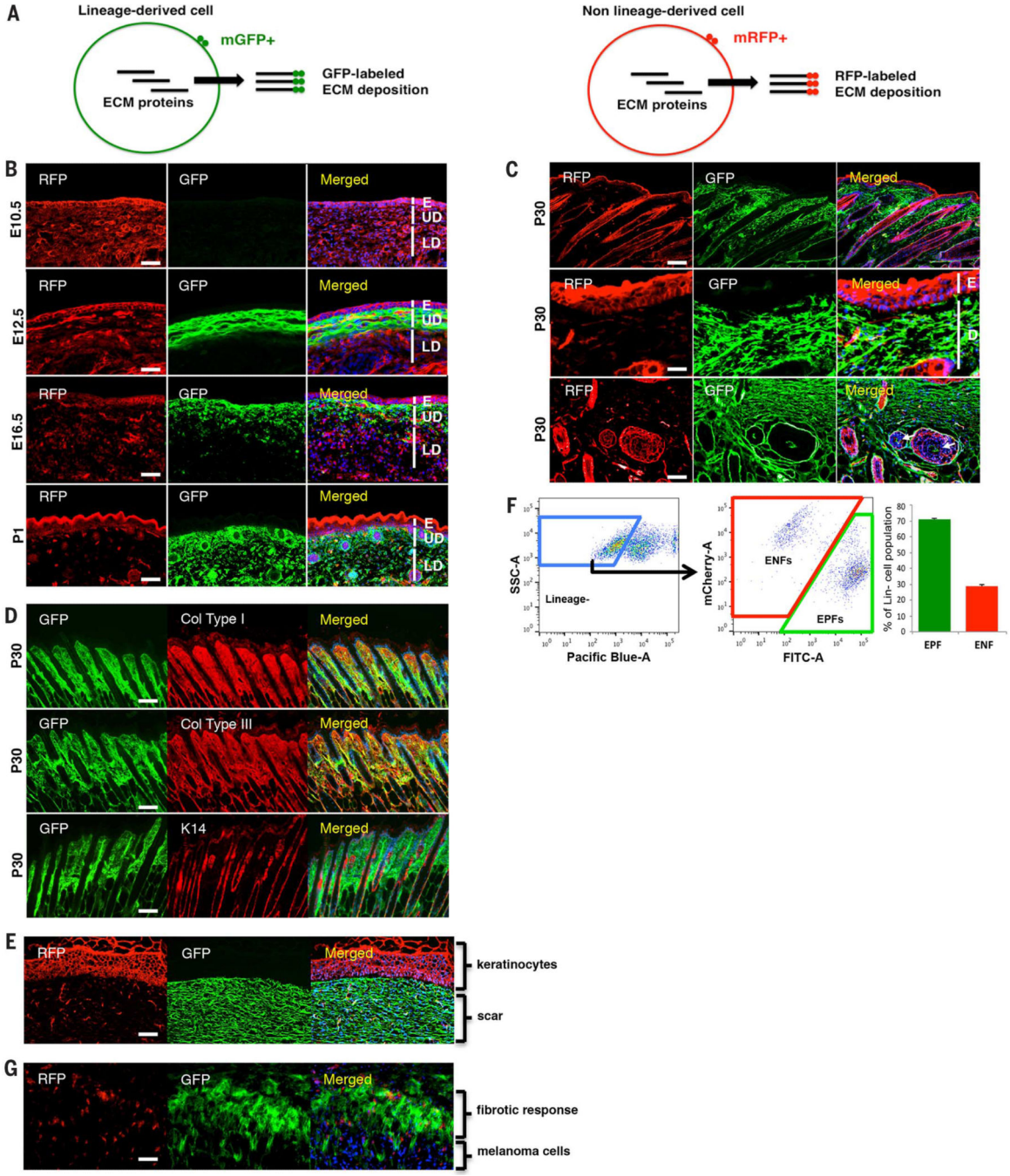

Fig. 3. EPFs are responsible for the bulk of connective tissue deposition in dermal scars and the reactive stroma of cutaneous melanoma

(**A**) Schematic showing how the mTmG system results in differential labeling of connective tissue depending on the cell type (EPFs or ENFs) responsible for connective tissue secretion. (**B**) Histologic analysis of dorsal skin harvested from E10.5 (top), E12.5 (one down from top), E16.5 (one up from bottom), and P1 (bottom) *En1*^{Cre};*R26*^{mTmG} mice. GFP (green) and RFP (red) are presented as individual channels and merged [includes DAPI (blue)]. Epidermis (E), upper dermis (UD), and lower dermis (LD) are marked with white bars in the

merged images. Scale bar, 300 μm. (**C**) Histologic analysis of dorsal skin harvested from P30 *En1*^{Cre};*R26*^{mTmG} mice. GFP (green) and RFP (red) are presented as individual channels and merged [includes DAPI (blue)]. Axial cut through hair follicles at 20x objective (top panel) and transverse cut at 40x objective (middle panel). Engrailed positive cells (GFP^{+}) within the dermal papillae/hair follicle bulge are identified by white arrows (bottom panel). Epidermis (E) and dermis (D) are marked with white bars in the merged images. Top: scale bar, 300 μm; middle: scale bar, 200 μm; bottom: scale bar, 100 μm. (**D**) Immunohistochemical analysis showing overlapping expression of collagen types I (top panel) and III (middle panel) with GFP fluorescence and nonoverlapping expression of keratin 14 (bottom panel) with GFP fluorescence on frozen sections of dorsal skin harvested from P30 *En1*^{Cre};*R26*^{mTmG} mice. Scale bar, 300 μm. (**E**) Histologic analysis of wounded dorsal skin from *En1*^{Cre};*R26*^{mTmG} mice at 12 to 14 days after wounding showing GFP-labeled ECM deposition and RFP-labeled fibroblasts, epidermis, and vasculature. Scale bar, 200 μm. (**F**) FACS analysis (left panel) and bar graphs (right panel) showing abundance of EPFs and ENFs in wounds of P30 *En1*^{Cre};*R26*^{mTmG} mice. (**G**) Histologic analysis of transplanted melanoma cells showing their associated stroma (primarily GFP^{+}) and vasculature (primarily RFP^{+}) in the dorsal backs of *En1*^{Cre};*R26*^{mTmG} mice at 30 days after transplantation. Scale bar, 100 μm.

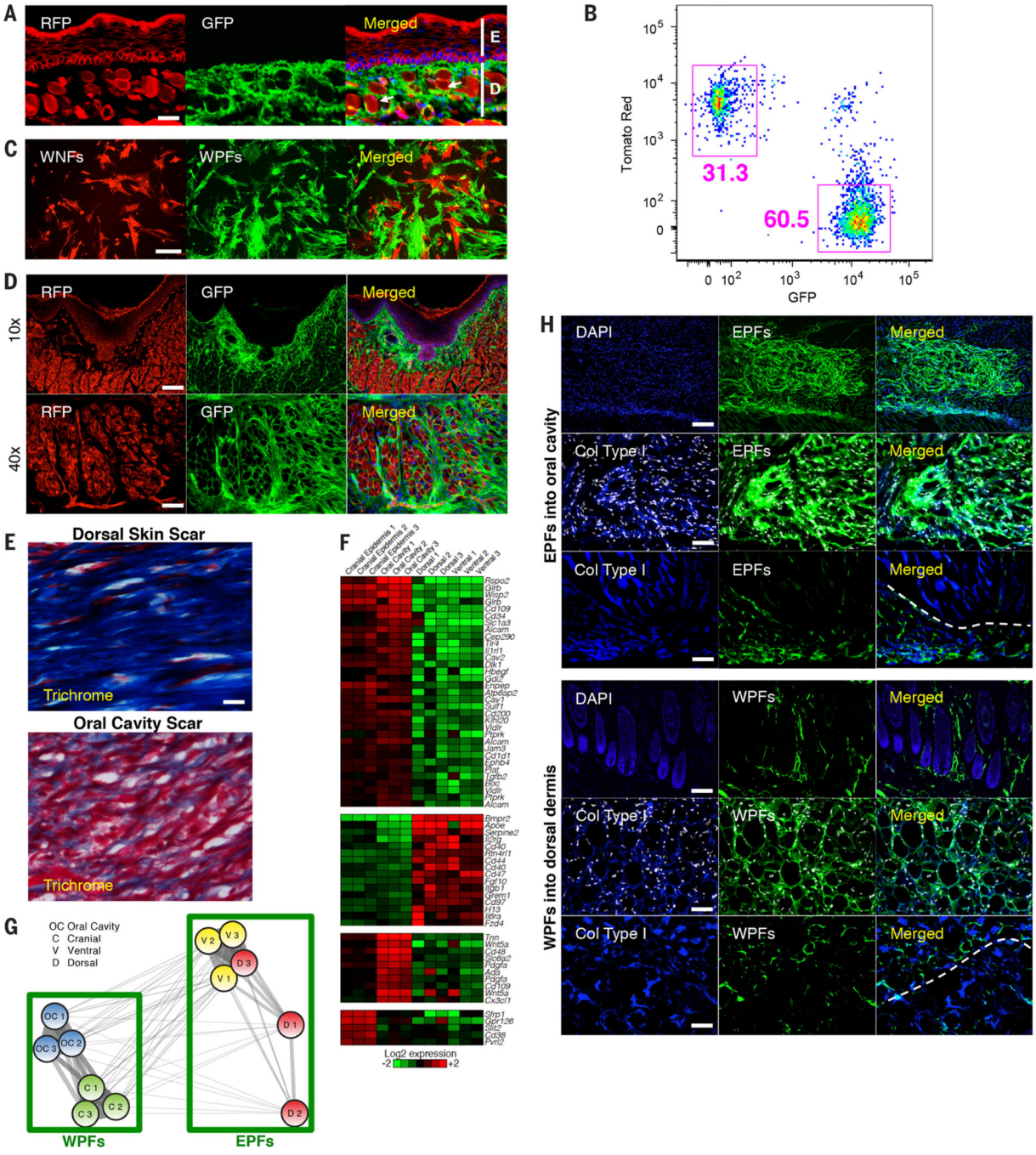

Fig. 4. Fibrogenic potential of dermal fibroblasts is cell-intrinsic

(**A**) Histologic analysis of oral dermis harvested from the buccal mucosa of P30 *Wnt1*^{Cre};*R26*^{mTmG} mice. Glandular structures in the oral dermis are identified by white arrows. Epidermis (E) and dermis (D) are marked with white bars in the merged images. Scale bar, 200 μm. (**B**) FACS analysis of WPFs and WNFs harvested from the oral dermis of P30 *Wnt1*^{Cre};*R26*^{mTmG} mice showing the relative percentage of each population within the oral dermis. (**C**) Cultured WPFs and WNFs portray characteristic fibroblast morphologies. Scale bar, 100 μm. (**D**) Histologic analysis of wounded oral dermis from *Wnt1*^{Cre};*R26*^{mTmG}

mice at 12 to 14 days after wounding showing GFP-labeled scar tissue, as well as RFP-labeled epidermis, vasculature, and adipose tissue in 10x (top) and 40x (bottom) magnification. Top: scale bar, 400 μm; bottom: scale bar, 100 μm. (**E**) Trichrome staining of oral cavity and dorsal scars at 14 days after wounding. Scale bar, 50 μm. (**F**) Heat map showing four representative clusters of differentially expressed genes from cultured WPFs (cranial dermis and oral dermis) and EPFs (dorsal dermis and ventral dermis). Although all probe sets were analyzed by the AutoSOME unsupervised clustering algorithm (22), for clarity, only surface markers are shown here. Detailed cluster results are provided in fig. S2A. (**G**) Fuzzy cluster network showing transcriptome-wide differences between oral cavity (WPFs), cranial (WPFs), dorsal (EPFs), and ventral (EPFs) fibroblast populations. Each node represents a microarray data set, and edges between nodes depict the pairwise similarity between fibroblasts as determined using AutoSOME (22), ranging from low similarity (thin and translucent) to high similarity (thick, with higher opacity). (**H**) Histologic analysis (GFP fluorescence and collagen type I staining) of EPFs from dorsal back of P30 $En1^{Cre};R26^{mTmG}$ mice transplanted into the oral cavity of $RAG\text{-}2^{-/-}$ double-knockout mice (top panels) and WPFs from the oral cavity of P30 $Wnt1^{Cre};R26^{mTmG}$ mice transplanted into the dorsal back of $RAG\text{-}2^{-/-}$ double-knockout mice (bottom panels). White dotted lines separate transplanted cells expressing collagen and native cells expressing collagen. 1st and 4th rows: scale bar, 300 μm; 2nd and 5th rows: scale bar, 100 μm; 3rd and 6th rows: scale bar, 200 μm.

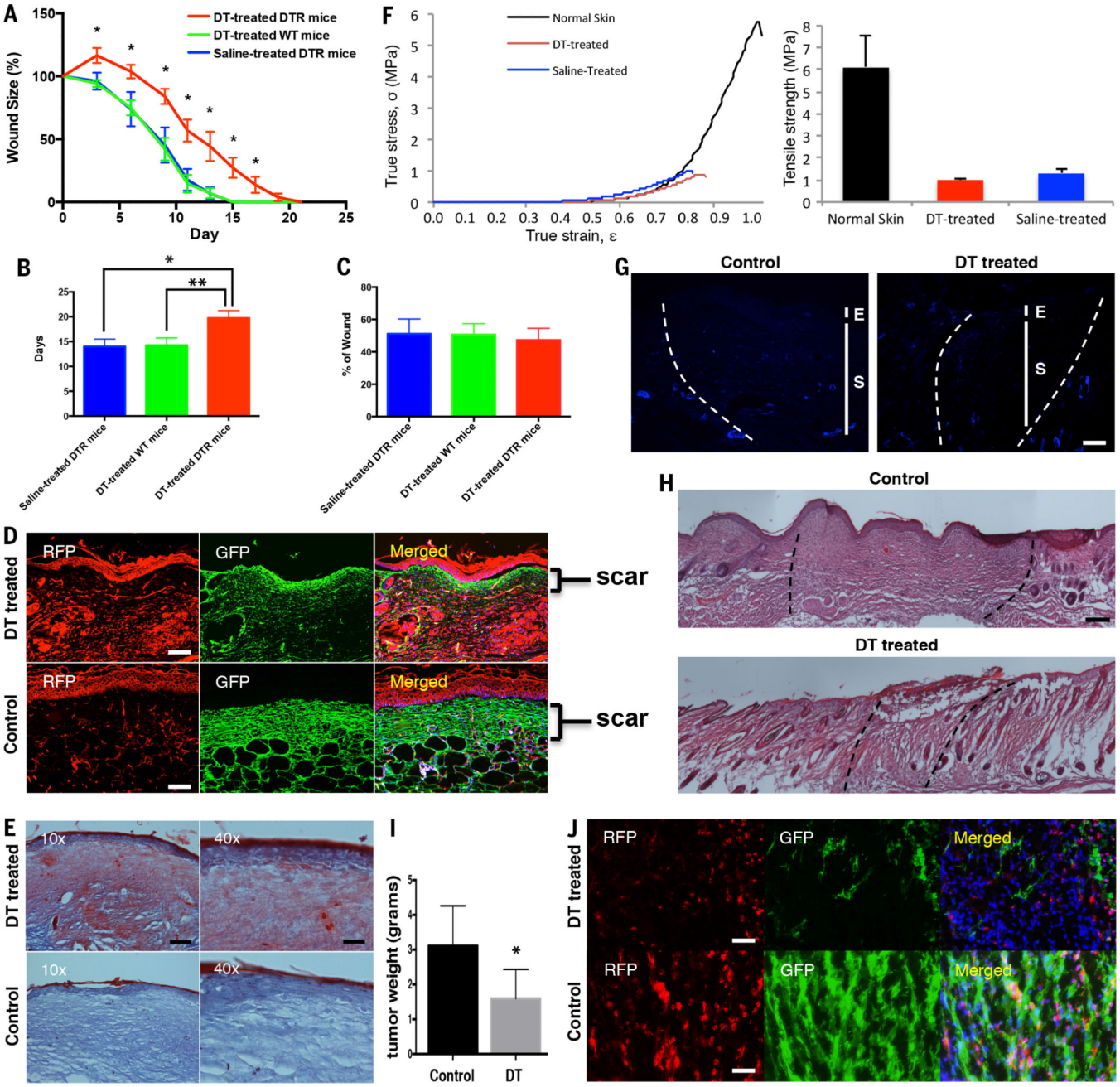

Fig. 5. DTR-based ablation of EPFs results in decreased connective tissue deposition (scar) after cutaneous wounding and reduced melanoma tumor size

(**A**) Wound healing curve plotted as a percentage of day 0 wound size versus days since wounding. DT-treated wounds ($n = 10$) (red) show significantly ($P < 0.01$) slower healing as compared with control wounds ($n = 10$) (green and blue). (**B**) Time to complete healing in DT-treated wounds ($n = 10$) (red) compared with control wounds ($n = 10$) (green and blue). (**C**) Scar size (area) measured as a percentage of the original wound area in DT-treated wounds ($n = 10$) (red) compared with control wounds ($n = 10$) (green and blue) showing no significant difference in scar. (**D**) Histologic analysis of GFP and RFP fluorescence in DT-treated wounds and control wounds. GFP (green) and RFP (red) are presented as individual

channels and merged [includes DAPI (blue)]. Scale bar, 200 μm. (**E**) Trichrome staining of DT-treated wounds and control wounds showing reduced collagen deposition in DT-treated (higher ratio of red:blue staining) as compared with control wounds (lower ratio of red:blue staining). Left: scale bar, 400 μm; right: scale bar, 100 μm. (**F**) Representative stress-strain profile (left) and ultimate tensile strength (right) of $En1^{Cre};R26^{mTmG};R26^{tm1(HBEGF)Awai}$ normal skin and fully healed wounds treated with DT and saline on days 21 and 15. (**G**) Immunofluorescent staining for adipocytes with FABP4 antibody showing that DT-treated wounds did not regenerate adipocytes compared with control wounds. Epidermis (E) and scar (S) are marked with white bars. In the control image, the healed wound is to the right of the white dotted line, and in the DT-treated image, the healed wound is in between the white dotted lines. Scale bar, 200 μm. (**H**) Hematoxylin and eosin (H&E) staining to visualize hair follicles showing that DT-treated wounds did not regenerate any hair follicles compared with control wounds. The healed wound is in between the black dotted lines. Scale bar, 500 μm. (**I**) Bar graph showing a significant ($P = 0.0413$) reduction in the weight of melanoma tumors at day 22 in DT-treated ($n = 7$) mice versus control ($n = 7$) tumors. (**J**) Histologic analysis of GFP and RFP fluorescence in DT-treated and control melanomas showing reduced EPF-derived connective tissue deposition in DT-treated as compared with control melanomas. Scale bar, 100 μm.

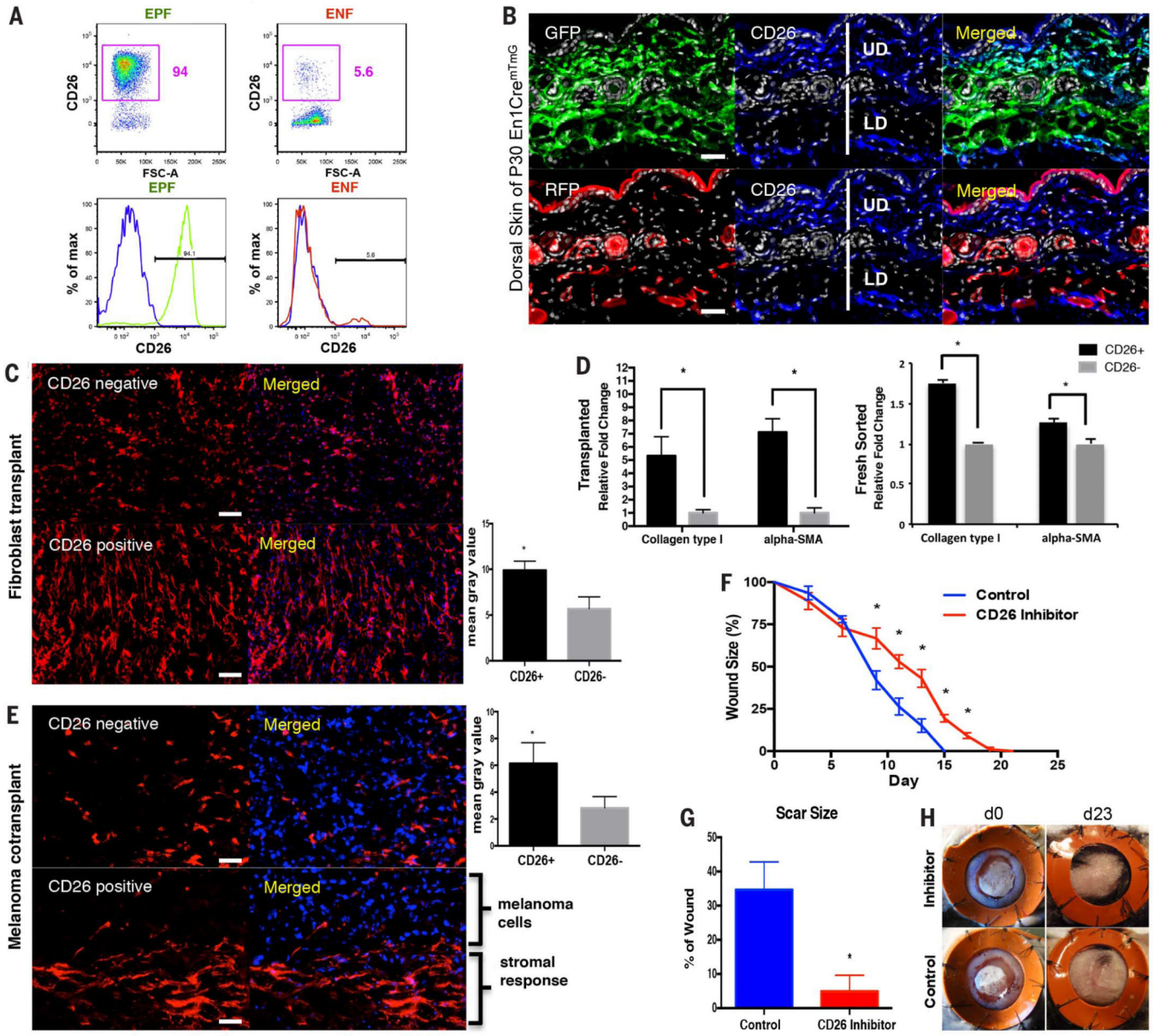

Fig. 6. CD26 allows enrichment of EPFs over ENFs, and its inhibition results in decreased connective tissue deposition (scar) after cutaneous wounding

(**A**) FACS analysis of CD26 expression on the surface of FACS-isolated EPFs and ENFs. (**B**) Immunohistochemical analysis of CD26 expression in the dorsal skin of *En1*^{Cre};*R26*^{mTmG} mice. White lines are marked on one of the images to denote upper (UD) and lower (LD) dermis. Scale bar, 200 μm. (**C**) Histologic analysis of FACS-isolated CD26^{-}Lin^{-} and CD26^{+}Lin^{-} populations from the dorsal skin of R26^{mTmG} mice transplanted via intradermal injection into the dorsal backs of *RAG-2*$^{-/-}$ double-knockout mice. Bar graph shows quantification of RFP fluorescence in CD26^{+}Lin^{-} (black) and CD26^{-}Lin^{-} (gray) grafts. Scale bar, 100 μm. (**D**) qRT-PCR analysis of collagen type I (P = 0.00957) and alpha-smooth-muscle actin (P = 0.0151) from FACS-isolated CD26^{+}Lin^{-} and CD26^{-}Lin^{-} cells. Right panel represents analysis of fibroblasts isolated from naïve dermis; left panel

represents analysis of fibroblasts isolated from wounded dermis at 10 days after transplant from $CD26^{+}Lin^{-}$ ($n = 3$) and $CD26^{-}Lin^{-}$ ($n = 3$) grafts [for graft histology, see (C)]. (**E**) Histologic analysis of FACS-isolated $CD26^{-}Lin^{-}$ and $CD26^{+}Lin^{-}$ populations from the dorsal skin of $R26^{mTmG}$ mice cotransplanted with B16 F10 mouse melanoma cells via intradermal injection into dorsal backs of $RAG\text{-}2^{-/-}$ double-knockout mice. Bar graph shows quantification of RFP fluorescence in $CD26^{+}Lin^{-}$ (black) and $CD26^{-}Lin^{-}$ (gray) melanomas grafts. Scale bar, 100 μm. (**F**) Wound healing curve plotted as a percentage of day 0 wound size versus days since wounding. CD26 inhibitor (diprotin A)–treated wounds ($n = 10$) (red) show significantly ($P < 0.01$) slower healing as compared with control wounds ($n = 10$) (blue). (**G**) Scar size (area) measured as a percentage of the original wound area in CD26 inhibitor (diprotin A)–treated (red) and control (black) wounds showing significantly reduced ($P = 0.0003$) scar size in CD26 inhibitor–treated wounds ($n = 10$) as compared with control wounds ($n = 10$) (blue). (**H**) Representative photographic images of wounds at day 0 and day 23 after wounding (complete healing and scar formation) in both control and CD26 inhibitor (diprotin A)–treated wounds.